Accepted Manuscript

Quarterly Journal of Engineering Geology and Hydrogeology

A single multi-scale and multi-sourced semi-automated lineament detection technique for detailed structural mapping with applications to geothermal energy exploration

Christopher M. Yeomans, Hester Claridge, Alexander J.L. Hudson, Robin K. Shail, Cees Willems, Matthew Eyre & Chris Harker

DOI: https://doi.org/10.1144/qjegh2022-051

To access the most recent version of this article, please click the DOI URL in the line above. When citing this article please include the above DOI.

This article is part of the Remote sensing for site investigations on Earth and other planets collection available at: https://www.lyellcollection.org/topic/collections/remote-sensing-for-site-investigations-on-earth-and-other-planets

Received 25 May 2022
Revised 1 November 2022
Accepted 17 November 2022

Supplementary material at https://doi.org/10.6084/m9.figshare.c.6309629

A single multi-scale and multi-sourced semi-automated lineament detection technique for detailed structural mapping with applications to geothermal energy exploration

Abbreviated title: *Multi-scale semi-automated lineament detection*

Christopher M. Yeomans[1*], Hester Claridge[2], Alexander J.L. Hudson[1,2], Robin K. Shail[1], Cees Willems[3], Matthew Eyre[1], Chris Harker[2]

[1]Camborne School of Mines, College of Mathematics, Engineering and Physical Sciences, University of Exeter, Penryn Campus, Penryn, Cornwall, TR10 9FE

[2]Cornish Lithium Ltd, Tremough Innovation Centre, Penryn Campus, Penryn, Cornwall, TR10 9TA

[3]Institute for GeoEnergy Engineering, Energy Academy, Heriot-Watt University, Edinburgh Campus, Currie, EH14 4AP

* correspondence (c.m.yeomans@exeter.ac.uk)

ORCID

CMY: 0000-0002-0364-451X, RKS: 0000-0001-7200-5124, CW: 0000-0002-4502-8598, ME: 0000-00025506674X

Abstract

Semi-automated algorithms incorporating multi-sourced datasets into a single analysis are increasingly common, but until now operate at a fixed pixel resolution resulting in multi-sourced methods being limited by the largest input pixel size. Multi-scale lineament detection circumvents this issue and allows increased levels of detail to be captured. We present a semi-automated method using a bottom-up Object-Based Image Analysis approach to map regional lineaments to a high level of detail. The method is applied to onshore LiDAR data and offshore bathymetry around the Land's End Granite (Cornwall, UK). The method uses three different pixel resolutions to extract detailed lineaments across a 700 km^2 area. The granite displays large-scale NW-SE fault zones that are considered analogous to those being targeted as onshore deep geothermal reservoirs (2-5 km in depth). Investigation of the lineaments derived from this study show along-strike variations from NW-SE orientations within granite to NNW-SSE within slate and reflect structural inheritance of early Variscan structures within Devonian slates. This is furthered by analysing these major structures for reservoir potential. Lineaments proximal to these broadly NW-SE features indicate a damage zone approximately 100-200 m wide is present. These observations provide a preliminary understanding of reservoir characteristics for

fault-hosted geothermal systems.

Supplementary material: Supplementary information on the OBAI methods and additional figures are available at https://doi.org/10.6084/m9.figshare.c.6309629

Introduction

Semi-automated lineament detection methods provide a rapid and robust means of mapping structural features at a multitude of scales. A geological lineament, defined as a mappable recti-linear or curvi-linear feature of a surface and distinct from adjacent patterns (O'Leary et al., 1976), can be mapped to infer faults or fractures within the subsurface. The semi-automated approach to lineament detection generally includes five steps: pre-processing; feature extraction; detection; linking; and vectorisation (Middleton et al., 2015). The increasing resolution of remotely sensed data allows more detailed lineament studies over larger areas, making a completely manual analysis more time-consuming. Therefore, semi-automated methods are becoming increasingly popular for practitioners.

There are a variety of published methods for semi-automated lineament detection available on a range of platforms, including tools within mainstream software packages such as PCI Geomatica and Seequent Oasis Montaj or bespoke algorithms (e.g. Rahnama and Gloaguen, 2014a,b; Middleton et al., 2015; Šilhavy et al., 2016; Masoud and Koike, 2017; Yeomans et al., 2019). Many of these are able to analyse multi-source data inputs, however, as yet no algorithm has attempted to combine multi-source and multi-scale input data. This would represent an important development in mapping in greater detail over larger areas.

Herein, we use an adaptation of the semi-automated bottom-up Object-Based Image Analysis (OBIA) method of Yeomans et al. (2019). We combine multi-scale and multi-source data from an onshore LiDAR elevation model and offshore bathymetry at three different pixel resolutions (5 m, 10 m and 20 m pixels) to evaluate lineament characteristics over an area of 700 km^2. This is complemented by two localised manual studies which validate the semi-automated method and demonstrate the level of structural detail. The study area is the Land's End peninsula and adjacent offshore areas in southwest England; the bedrock

geology comprises the Land's End Granite and its Devonian host rocks. It has been selected due to its importance for understanding NW-SE fault zones that are currently being targeted farther east in Cornwall as fault-controlled deep geothermal reservoirs (United Downs Deep Geothermal Power Project near Redruth and the Eden Geothermal Project, St Austell). The Land's End area is an ideal locality to study these NW-SE fault systems due to the accessibility of granite coastal exposures and the quality of bathymetric data. Exposed bedrock in offshore areas reveals a detailed fault network and these areas can be mapped at high resolution to give a representative model of the underlying fault network that may otherwise be obscured in onshore areas.

Lineament networks have played an essential role in defining geothermal systems in other parts of the world such as the Rhine Graben (Bertrand et al., 2017) and in Scotland for coal mine geothermal resources (Andrews, 2020). In southwest England, the viability of major NW-SE fault systems as reservoirs for deep geothermal energy is being explored. Previous work in southwest England has investigated NW-SE structures but has highlighted complexity with other orientations such as NNW-SSE and NNE-SSW features (Nixon et al., 2012) and ENE-WSW fault-controlled vein (lode) systems further east (Alexander and Shail 1995, 1996; Shail and Alexander, 1997). This work details initial attempts to understand the nature of these fault systems at a regional scale. These structures and their interactions with NW-SE systems are investigated based on their host rock and their distance from manually digitised fault traces. We assess the appropriateness of semi-automated and manual approaches for lineament mapping as a precursor to future reservoir modelling and highlight the potential for algorithmic selection bias in semi-automated methods. Orientation data is used to identify target structures and derive an estimate of "damage zone width", however, further characterisation of the reservoir (e.g., connectivity and flow modelling) is beyond the scope of this work.

Geological setting

The Upper Palaeozoic geology of southwest England (Figure 1) comprises low-grade regionally metamorphosed Devonian-Carboniferous greywacke-mudstone sedimentary successions, with minor intrusive mafic igneous rocks, that were deformed during the

Variscan Orogeny (Leveridge and Hartley, 2006). These were later intruded by the Cornubian Granite Batholith in the Early Permian (Scrivener, 2006). Three regional deformation events (D1-D3) are recognised (Alexander & Shail, 1995,1996). D1 and D2 structures developed in an NNW-directed thrust-fold belt during Variscan continental collision following the closure of the Rheic-Rhenohercynian Ocean. D3 structures formed during latest Carboniferous to Early Permian post-Variscan regional extension during which thrust faults were reactivated as top-to-the-SSE extensional faults and new higher-angle ENE-WSW striking extensional faults formed (Alexander and Shail, 1995; Shail and Alexander, 1997; Shail and Leveridge, 2009; Alexander et al., 2019).

INSERT FIGURE 1 (regional geology)

Early Permian magmatism was, in part, synchronous with regional D3 extension and is largely represented by the Cornubian Batholith that was emplaced between 293-275 Ma (Chen et al., 1993, Chesley et al., 1993; Scrivener, 2006; Simons et al., 2016). The Land's End Granite study area is located at the westernmost end of the mainland, although it is worth noting the batholith continues some 100 km offshore for a similar distance westward across the Cornubian Ridge (Evans, 1990). A magmatic-hydrothermal tungsten-tin-copper-zinc orefield was developed contemporaneously with batholith construction and was overwhelmingly fault- and joint- controlled (Chen et al., 1993, Chesley et al., 1993); present in the study area as the St Just Mining District. Extensional fault-controlled vein systems (lodes) are typically ENE-WSW to E-W oriented, reflecting NNW-SSE to N-S extension, and formed synchronously with steeply-dipping NNW-SSE strike-slip transfer faults. The latter stages of mineralisation, presumed to be associated with the youngest magmatic episodes, are commonly oriented NW-SE to N-S and may reflect a change in regional stress (Shail and Alexander, 1997). The development of Early Permian ENE-WNW to E-W oriented extensional fault systems in the granites and their host rocks was contemporaneous with the formation of extensional sedimentary basins that host Permian 'red bed' successions (Evan, 1990; Alexander et al., 2019).

The subsequent structural evolution of fault networks during the Mid-Permian to Mid-Triassic is poorly constrained but two minor episodes of intraplate shortening are identified

(Shail and Alexander, 1997). Regional ENE-WNW extension during the Triassic brought about the extensional reactivation of Early Permian NNW-SSE transfer faults and development of new faults (Shail and Alexander, 1997) and a regional Middle Triassic episode of basinal brine migration through the NW-SE to NNE-SSW extensional fault systems. The resultant basement-hosted 'cross-course' veins offset earlier Permian magmatic-hydrothermal lodes (Scrivener et al., 1994; Gleeson et al., 2000, 2001).

Following the Triassic cross-course event, there is little constraint on the onshore structural evolution until the Cenozoic. An Oligocene intraplate strike-slip tectonic regime resulted in both dextral and sinistral reactivation of NW-SE faults, with displacements of up to several kilometres, along the Sticklepath-Lustleigh Fault Zone in the east of the region (Holloway and Chadwick, 1986).

The Land's End Granite and surrounding area

The Land's End Granite is the youngest of the granite plutons at c. 274-279 Ma (Chen et al., 1993; Chesley et al., 1993) having been intruded into the Upper Devonian Mylor Slate Formation of the Gramscatho Group (Figure 2A). It forms the most westerly mainland exposure of the Cornubian Batholith and provides consistent exposure of the granite and its margins in coastal outcrop. The present-day shape of the pluton is unusual compared to the other plutons in southwest England, characterised by a distinct geomorphology controlled by regularly spaced NW-SE oriented valleys and well represented in Figure 2B. These features extend offshore, and are observable in the seafloor, where the bedrock is Gramscatho Group. The submerged outcrop provides a highly detailed surface upon which to study fracture networks and trace these back to onshore areas where outcrop is more limited. Offshore areas are susceptible to sediment cover, which obscures the desired bedrock exposure, and the occurrence of sand waves upon these sediments can cause false positive results in semi-automated lineament studies. However, these are not extensive in the area selected and have been mitigated during post-processing.

INSERT FIGURE 2 (local geological)

Lineament detection methods

As datasets increase in coverage and resolution, semi-automated lineament detection becomes a more efficient choice to the practitioner for rapid, objective lineament mapping. Built-in tools to mainstream software are commonly applied but there is an increasing prevalence of bespoke algorithms designed for use within different programming languages such as MATLAB (Rahnama and Gloaguen, 2014a,b), Python (Šilhavy et al., 2016; Karimi and Karimi, 2017) and eCognition's Cognitive Network Language (Middleton et al., 2015; Yeomans et al., 2019). Others can operate as plug-ins to existing GIS software such as the GeoTrace toolbox for QGIS (Thiele et al., 2017).

Many of these semi-automated methods achieve their results through very different approaches, be it through targeting edges, or minima in the data, or through different methods such as pixel-based compared to object-based (e.g. Sukumar et al., 2014; Rahnama and Gloaguen, 2014a,b; Middleton et al., 2015). Regardless, the key to a successful semi-automated algorithm is effective feature extraction to best enhance desirable structures and minimise the inclusion of spurious lineaments. Various feature extraction methods exist, and it is beyond the scope of this study to discuss them all, however, the application of the tilt derivative to LiDAR data (Middleton et al., 2015) and to bathymetry data (Yeomans et al., 2021) has proven highly effective. A comparison of the tilt derivative to more classical enhancement techniques, such as the Gradient, Sobel and Laplacian filters as well as the hillshade transform, found that the tilt derivative was more successful at creating continuous lineaments that were consistently sensed across an entire region of interest (Yeomans et al., 2021).

Despite the focus on semi-automated methods, manual analyses are not without merit. Smaller manual studies, over representative subsets of a much larger study area, can help validate semi-automated lineament sets. Alternatively, it may be necessary to fill in data gaps using another dataset that may not be available for the whole area or be impractical as input to a semi-automated algorithm. It should be noted that subjective bias is easily introduced and, over large areas, becomes time-consuming and lacks reproducibility (Masoud and Koike, 2006; Scheiber et al., 2015). However, it is suggested by Andrews et al.,

(2019), that reference to field observations can reduce the subjective bias. Furthermore, manual analyses are widely considered to be better for topological analysis of fracture connectivity. Semi-automated networks are often highly segmented resulting in short trace lengths and fewer connected branches and therefore are inferior for connectivity studies.

To date, lineament detection studies, semi-automated or manual, have largely focused on augmenting their results by incorporating multi-sourced datasets. The approach has found success where lineaments that may have different signatures can be detected across different datasets and be incorporated into a final analysis. Some semi-automated methods do this within a single analysis (e.g., Masoud and Koike 2011, 2017; Yeomans et al., 2019). Some studies have looked at different resolution datasets (e.g., Meixner et al., 2017) but not within a single analysis. Combining different resolution data to map larger areas in greater detail is presently the frontier of lineament detection methods.

Data and Methods

Three lineament sets are generated within this study area. A semi-automated approach using an adaptation of the bottom-up OBIA method by Yeomans et al. (2019) is conducted to detect lineaments across the whole region of interest and a workflow is presented in Figure 3A. Methods for data processing and lineament detection are presented as well as a detailed account of the required post-processing. A smaller manually digitised lineament set is generated to validate the semi-automated analysis. Both of these lineament sets are generated from a combination of onshore LiDAR and offshore bathymetric data. A third set is generated to fill in the data gap between the onshore and offshore datasets using aerial photography.

INSERT FIGURE 3 (workflow + masks)

Data

The LiDAR data were collected as part of the collaborative Tellus South West project, and the LiDAR survey was conducted by the British Antarctic Survey between July and August 2013. The LiDAR dataset has a spatial resolution of 1 point per meter and the data are accurate to 10 cm (both horizontal and vertical accuracy) (Gerard,2014). The Digital Terrain

Model (DTM) was downloaded from the Centre of Ecology and Hydrology repository in ascii grid format at 1 m pixel resolution. The onshore part of the study area covers approximately 227 km^2.

Bathymetric data were downloaded from the Admiralty Data Portal under an Open Government Licence and included five blocks of multi-beam bathymetric data collected between 2008 and 2016. These were downloaded in raster format at 2 m pixel resolution. The multi-beam bathymetry data in the study area revealed an expansive area of submerged bedrock offshore. The data extend from the nearshore environment some 10 km from the shoreline and have an approximate coverage of 423 km^2.

Proximal to onshore areas, a roughly NE-SW trending area of sediment covered seafloor is present resulting in no bedrock for lineament mapping. More localised patches of seafloor cover are present in other areas but are often small and not detrimental to the overall dataset. In rare, but spectacular cases, sand waves have formed on the seafloor and have the potential to cause artefacts in the data. These potentially problematic areas are included in subsequent analysis and dealt with in the post-processing.

The immediate nearshore areas can lack data coverage, likely due to tides, poor sea conditions during acquisition or treacherous waters making acquisition too dangerous. This can lead to a gap when combined with the onshore LiDAR and result in the phenomenon referred to as the 'white ribbon' (Mason et al., 2008). To mitigate missing data in the onshore-offshore elevation model, optical aerial photography of the coastal zone and immediate nearshore was downloaded from the EDINA Digimap repository under an educational licence. The initial data were supplied in 3-band raster format at 25 cm pixel resolution. This dataset was used to supplement lineament mapping in the area and attempt to bridge data gaps where they exist.

Object-Based Image Analysis

Object-Based Image Analysis (OBIA) tools have been increasingly applied in recent years. The approach makes use of raster input datasets to identify groups of pixels that are defined

as “image objects” through a process of image segmentation. The approach can use a variety of segmentation methods including top-down (thresholding) and bottom-up (merging) to identify image objects (Diamant, 2004; Dragut et al., 2010; Eisank et al., 2014). These image objects are linked through a topology that describes their spatial relationship to one another and allows the calculation of geometric properties and internal statistics based on the subset pixels. The approach provides a profusion of metrics to compare, merge and/or classify image objects.

OBIA has been increasingly used in lineament detection studies such as Mavrantza and Argialas (2006), Rutzinger et al. (2007) and Marpu et al. (2008) but most recently through the workflows developed by Middleton et al. (2015) and Yeomans et al. (2019). A key step in these studies is the use of the tilt derivative transform for initial feature extraction prior to applying an OBIA workflow. An initial top-down OBIA method by Middleton et al. (2015) made use of airborne magnetic and LiDAR data separately to generate lineament networks. This approach was developed by Yeomans et al. (2019) to integrate multiple datasets (airborne magnetic, LiDAR and radiometric data) into a single workflow and produce a composite lineament network. A complementary bottom-up method was also produced, which sacrificed some detail in metadata and lineament length but was computationally more efficient and is therefore considered more desirable for larger datasets (Yeomans et al., 2019). Other feature extraction methods have been tested on bathymetric data by Yeomans et al. (2021), exploring the use of gradient and Laplacian filters and the hillshade transform in comparison to the tilt derivative, but were found to underperform where steep gradients (e.g., palaeocoastlines) in the seafloor were present in the data. It is assumed that this extends to subaerial steep gradients such as present-day coastlines.

Data processing

The five bathymetric data blocks were initially converted from Bathymetric Attribute Grid (.bag) files to a Geotiff format and merged into a single dataset. A visual inspection revealed that, despite the use of near-shore CCO data, some missing data were still present in the final product. Further, it was noted that the join between nearshore Channel Coastal Observatory (CCO) data and UKHO bathymetric data had a minor step. This is likely due to the higher resolution acquisition of the CCO data and minor differences between the

Admiralty Chart Datum and Ordnance Datum to which these datasets are reduced for UKHO and CCO, respectively. The step was noted and revisited during post-processing.

The merged data were resampled to 5 m pixels prior to clipping to the study area and forms the first input layer to the semi-automated lineament detection. To generate the two other input layers, the LiDAR data were integrated with the bathymetric data to combine a single elevation model which was subsequently resampled to 10 m and 20 m pixel resolution.

Once the three layers were prepared, the data were exported to ascii format and imported into the Oasis Montaj 9.7 package where the data were processed using the tilt derivative transform within the MAGMAP GX package. The tilt derivative, commonly applied to potential field data such as gravity and magnetic datasets, can be applied to non-potential field data by calculating the vertical derivative by convolution as illustrated in Equation 1.

$$TDR = \left(\frac{\frac{\partial T}{\partial z}}{\sqrt{\left(\frac{\partial T}{\partial x}\right)^2 + \left(\frac{\partial T}{\partial y}\right)^2}} \right) \quad (1)$$

where *TDR* is the tilt derivative, *T* is the target pixel; *x*, *y* are horizontal derivatives; and *z* is the vertical derivative.

The tilt derivative is a useful tool for lineament detection methods because it normalises the magnitude of features preserving minor lineaments in the presence of larger features (Miller and Singh, 1994; Verduzco et al., 2004; Fairhead and Williams, 2006). It also produces more continuous features where the feature may show minor variations along strike (Verduzco et al., 2004) and normalises the data using the arctangent where the zero contour passes over or near the edge of a feature (Miller and Singh, 1994).

Lineament detection

The use of three input datasets processed at different resolutions (5 m, 10 m and 20 m pixels) allows the capture of a range of lineaments that may display different characteristics.

This is particularly effective for identifying fault traces that have a different geomorphologic expression in onshore areas, which may be heavily incised, compared to offshore areas. Additionally, it allows the capture of more detailed lineament networks observable in the seafloor which are masked onshore by soil cover.

The lineament detection workflow applied in this study develops the bottom-up methodology first outlined by Yeomans et al. (2019). The workflow is outlined in Figure 3 which adapts the line extraction steps to include different resolution datasets that are tuned to extract lineaments based on the observable geomorphological features. The workflow is conducted in the eCognition software package using the Cognitive Network Language.

Firstly, lineaments are extracted using a rectangular kernel comprised of three stripes oriented in the long axis of the kernel. The kernel can be rotated and iterated through 360° and for this study an interval of 5° was selected. A lineament is identified using the central stripe of pixels and is given a weight based on the similarity on either side of the central stripe using the border two stripes. The majority of lineaments in the study area are assumed to be represented by minima in the data where they have been preferentially eroded. The output of the line extraction is a “lineness” raster for each input dataset, all of which are subsequently merged (giving equal weight) into a single raster.

Following line extraction, bottom-up image segmentation is employed using the *multi-resolution* segmentation tool. The image is divided into many, differently sized image objects which are subsequently merged based on their spectral, statistical, textural, geometric or topological properties. The process also incorporates cleaning steps that remove spurious image objects. Furthermore, this analysis allows the designation of major and minor lineaments in the metadata. The threshold for this is user defined and is based on the relative similarity of features (as defined by the kernel during lineament extraction) rather than a geological measure of importance. Further notes can be found in the Supporting Information.

The final step in the lineament detection processes is to convert image objects to vector format. Given the polygonal nature of an image object, these are simplified to vector lines

to produce a skeleton of the image object and a main line (principal axis) of the image object. The two forms allow the main lineament to be identified but also preserve branches should significant lineaments be conjoined. Given that only NW-SE features have been targeted in this instance, the main line vector file was taken forward.

Post-processing

The output vector lines have been post-processed to include segment length and orientation. These were calculated based on the polyline geometry within a GIS where the orientation of polylines was calculated in the range 0-179°. Furthermore, a spatial join was used to create two fields, one for bedrock type and another for location in the onshore or offshore environment. These were appended to the attribute table for the data. Full details of these methods are given in the Supporting Information.

Due to the semi-automated nature of the lineament detection algorithm, due diligence was conducted to ensure lineament quality for both onshore and offshore lineaments. Upon visual inspection it was apparent that areas of sediment cover and sand waves in the bathymetric data had generated artefacts during the transformation using the tilt derivative. Therefore, post-hoc removal of potential spurious lineaments was conducted using the approach developed by Yeomans et al. (2021) that implements the Terrain Ruggedness Index (TRI) to map areas of sediment cover. The TRI is used to identify smooth areas which are assumed to represent sediment cover where the submerged outcrop on the seafloor is rough. These areas can be preferentially selected by using a threshold. In this study, the 5 m resolution offshore data were used to calculate the TRI layer which was normalised to 0-1 and a threshold of 0.0025 was selected using a heuristic approach. This threshold was used to generate a mask (Figure 3B) that selected all lineaments wholly within the mask and removed them.

Sediment cover in the bathymetric data cannot be fully addressed through a TRI mask. Due to the presence of sand waves in some areas causing a ripple effect on the surface, the “smoothness” criteria was not a panacea. Therefore, a manual mask was created that identified 11 areas of sand waves and these were removed where lineaments fell wholly within the mask. Additionally, a step in the bathymetry data was noticed around the

southern extent of the study area, likely pertaining to a significant time gap between acquisitions. The lineaments generated immediately over the join between the two bathymetric datasets were manually removed by directly editing the shapefile.

Further post-processing of the onshore areas was conducted to remove field boundaries and roads. In Cornwall, these can be particularly problematic to semi-automated lineament detection due to the presence of “Cornish hedges”, tall granite walls covered with earth, which result in a similar feature to desirable lineaments. It is possible that hedges and field boundaries removed in this step follow subtle geological features and result in a loss of data, however, due to their problematic response and small scale, the accurate mapping of these features is unlikely to be reliable. In this case, it was noticed that most of these spurious lineaments are generated from the 10 m resolution layer whereas the 20 m resolution layer had few errors. On this basis, the 20 m resolution layer was smoother where target values in the tilt derivative would be smeared out and less susceptible to the misidentification. As a consequence, to identify these artefacts and remove them, post-processing began by selecting all onshore lineaments and filtering to reduce the population based on lineaments with a length < 300 m and with a TDR value > -0.5 in the 20 m resolution layer (i.e., lineaments with TDR values (t) in the range $-0.5 > t >= 1.57$ that are < 300 m in length were removed). As an additional step, all lineaments with a length < 50 m in onshore areas were also removed.

The extensive post-processing steps described here demonstrate the importance of due diligence when processing large datasets from multiple sources. Careful examination of the lineament set over the region of interest identified likely spurious features caused by a variety of artefacts, each of which required a different approach to remove and ensure quality. Of the original 28350 lineaments derived from the OBIA algorithm, a total of 10009 were removed leaving a final lineament population of 18341 to be taken forward for analysis; a full breakdown is given in Table 1. This is a high proportion of false positive lineaments and a potential drawback of the semi-automated method when applied to high resolution data. However, careful post-processing to identify false positives and their defining spatial or geometrical characteristics can objectively remove spurious lineaments.

INSERT TABLE 1 (removed lineaments)

Manual mapping

Manual lineament mapping has been conducted twice in this study to complement the semi-automated methods. An area of7 km^2 was selected that demonstrates the detail within the offshore data that is beyond the scope of being captured by the semi-automated method used by this study. The study also manually digitised lineaments that were present within the white ribbon using aerial photography. This lineament set attempts to bridge the data gap between onshore LiDAR and offshore bathymetry and provide insight into lineament populations at even higher resolution.

Offshore environment

The sub-area of interest is a 7 km^2 region straddling the west coast of the Land's End peninsula between Botallack in the southwest and Morvah in the northeast. The fault network was mapped from high-resolution multi-beam bathymetry of the offshore region and airborne LiDAR data into the onshore portion of the area at a pixel resolution of 2 m. The majority of the submerged bedrock is inferred to be Mylor Slate Formation with the exception of bedrock immediately offshore of the Land’s End Granite coastal exposure (BGS Geology, 2000; Goode and Taylor, 1988).

The multi-beam bathymetry and LiDAR data were imported into a GIS for interpretation where a hillshade transformation was applied to accentuate fault traces. It is common practice to generate two orthogonal hillshades and map lineaments in both illuminations to minimise bias (Scheiber et al., 2015). For this study, illumination source azimuths of 315° and 225° with an altitude of 45° were used for the transformation. Analysis of the structures within this sub-area was conducted manually, by hand-digitising lineaments at a consistent scale 1:5000. The scale was chosen as a reflection of Tobler's rule where a minimum map scale is determined by multiplying the pixel resolution by 2000. The 1:5000 scale was therefore chosen as close to this minimum map scale but also to reflect common mapping scales.

Nearshore environment

The nearshore environment is often a problematic area when linking between onshore and offshore datasets. The process of merging a digital elevation model with a bathymetric dataset often results in a gap in the data; the so-called white ribbon (Mason et al., 2008). The missing data in this area can vary depending on the data source and a workflow by Leon et al. (2013) attempted to create a seamless elevation model over areas that have multiple spatial and temporally separate elevation datasets. Other studies have used field observations and geological mapping to supplement the data gap (Sanderson et al., 2017; Westhead et al., 2018). Whilst data acquisition in this zone is possible, it is often costly and requires careful planning. Neither have been permissible to-date as a continuous study around the west Cornwall peninsula, therefore in this study, aerial photography was used to map the nearshore, wave-cut platform and immediately onshore areas.

In this study area, the white ribbon is not pervasive around the whole coastline. It is largely constrained to the west and north coasts which have more inclement weather and have the least protection in periods of high swell compared to the south coast. Mapping of the nearshore environment was conducted around the entire coast in the study area. Aerial photography at 25 cm pixel resolution, available from EDINA Digimap resources on an Education and Research licence, was downloaded and a 250 m buffer around the coast was used to extract and mosaic the relevant image tiles. Lineaments were then manually digitised at a fixed scale of 1:500. Manual mapping was necessary due to the complexity of the image with highly varied outcrop shapes including steep slopes and wave-cut platform; the changing environment between shallow water and vegetated areas affecting the image texture; and the difficulty of removing the effects of shadows. However, these aspects must also be considered during interpretation of the derived lineaments as they cause selection biases (Shipton et al., 2019).

Results and Discussion

Herein, the three different lineament networks generated in this study are presented. This study has examined the influence of bedrock geology and discuss the geological interpretations that can be made using all three lineament networks. Additionally, orientation analysis was used to estimate damage zone widths relating to major NNW-NW

structures that may be potential targets for fault-controlled geothermal reservoirs. Finally, we compare and contrasts the lineament networks and discuss the benefits and limitations to semi-automated and manual analyses.

Rose diagrams presented herein have been created using the guidelines laid out by Sanderson and Peacock (2020) for equal-area wedge rose diagrams. These diagrams are superior to the conventional equal-radius approach because it better represents more subtle trends and allows for a more robust comparison between networks with different populations of lineaments. For comparison, equal-radius rose diagrams are included within the Supplementary Information and illustrate the overemphasised principal orientations.

Comparing three lineament networks

The semi-automated lineament network (Figure 4A) shows the whole study area, B the equal-area rose diagram for the lineament population and C and D highlight the greater density of lineaments mapped in the offshore bathymetry. Results from the offshore manual analysis (Figure 5A) show the extent of the network and area of interest in, equal-area rose diagram (Figure 5B) and the complexity of the network, and the structural evolution are illustrated through Figure 5C-E. Lineaments from the white ribbon lineament set are presented in Figure 6A with corresponding equal-area rose diagram (Figure 6B) and sub-panels highlighting nuances in the lineament network (Figure 6C-F). Comments on the network and orientations for all three analyses are given in Table 2.

INSERT FIGURE 4 (semi-automated lineaments – red)
INSERT FIGURE 5 (manual offshore lineaments – orange)
INSERT FIGURE 6 (white ribbon lineaments – green)
INSERT TABLE 2 (lineament summary)

It is worth noting that in Figure 4, onshore areas are dominated by terrestrial drainage compared to offshore areas where the exposed bedrock was likely formerly a subaerial platform (Healy, 1996; Waller and Long, 2003). This has been submerged and stripped of vegetation and superficial sediment and may have subsequently been modified by wave-

dominated processes in the marine environment. The result means a much higher density of lineaments are able to be sensed in the offshore areas which undoubtedly exist onshore but are not exposed and do not create a geomorphological signature that can be sensed in the data. Furthermore, there are some cases that can be seen in Figure 4C and 4D where some structures may have not been detected and is likely due to a lack of consistent signal causing small segments that were subsequently removed during the cleaning stages.

In Figure 5, there is a predominant orientation of NNW-trending lineaments, but NE-trending features are also prominent (Figure 5D). The relationship between these systems is difficult to unpick from lineament analysis alone but both main sets appear to mutually cross-cut each other suggesting multiple reactivation episodes, as highlighted in Figure 5E.

Figure 6C-F illustrate the variation that exists in the lineament population at this small scale. Figure 6C shows the prevalence of lineaments that can be detected here from aerial photography. The digitised lineaments in this area do not appear to reflect the orientations of those detected in the semi-automated lineament set. This may indicate that at more local scales, the lineament network is more complicated and may represent small relays or transfers or a broader damage zone. Figure 6D shows regular sets of NW-SE tending lineaments which reflect those detected in the semi-automated set. The manual analysis also contains NNW and NE-ENE orientations that intersperse the NW sets but are not apparent in offshore or onshore areas within the semi-automated method. Figure 6E highlights where the manual lineaments populate the white ribbon in the data and show a complex mix of WNW-ESE, NE-SW and N-S features. This area demonstrates a broad agreement with the general trends observed in the semi-automated lineament set. Figure 6F highlights that major NW-SE lineaments extend from onshore into offshore areas. Between these features, few lineaments are detected in the bathymetry or LiDAR, but manual coastal interpretations show that a complex network exists between large scale features, reflecting the complexity highlighted in Figure 6C.

Geological interpretations

Bedrock controls on lineament orientation

Lineaments in all three sets show multimodal populations, some more subtle than others. These modal groupings may be explained by different bedrock types and reflect the protracted structural evolution of the area. For simplicity, the rocks within the study area have been divided into “granite” and “slate” subdivisions as these are the dominant rock types.

In Figure 7, equal-area rose diagrams are presented that depict the granite and slate subdivisions for the semi-automated lineament set. There is a clear change in modal trends between granite and slate subdivisions. The granite subdivision (Figure 7A) displays a strong NW-SE trend that is much more diffuse in the slate subdivision (Figure 7B) and may reflect a mechanical control on fault propagation through the slate compared to the granite. Both subdivisions express a strong lineament grouping that trend approximately ESE-WNW. These observations are explored further through the different environments within which one can sense these lineaments.

INSERT FIGURE 7 (rose diagrams granite-slate)

Figure 8 highlights the differences between lineaments detected in an onshore versus anoffshore environment. Figure 8A,B present lineaments detected over onshore areas for both the granite and slate subdivisions, respectively. It can be seen here that granite lineaments have an intense modal population of NW-SE trending features with a more subdued ESE-WNW trend. In comparison, the slates show a dominant ESE-WNW trend but, perhaps surprisingly, mimic the NW-SE trend observed in the granite subdivision. The slates also demonstrate other orientations of lineaments such as NNW-SSE and NE-SW features that are less prevalent in the onshore granite set. When compared with offshore areas in Figure 8C,D, the lineaments in the offshore granite subdivision have a noticeably subdued NW-SE trend and are dominated by ESE-WNW trending features. Again, the ESE-WNW group is observed in the offshore slate subdivision and the broad grouping in the NW-SE quadrants that was noted in Figure 9B is also apparent but with a stronger skew towards a

NNW-SSE trend.

INSERT FIGURE 8 (rose diagrams granite-slate by onshore-offshore)

Implications for ESE-WNW structures

The lineament data in both the semi-automated and manual offshore networks capture an ESE-WNW set that represents either bedding-parallel faults or recessive features related to the erodibility of different sedimentary packages. The E-ESE orientation contrasts with the dominant ENE-E trend of bedding within the Devonian sedimentary successions to the east of the Land's End Granite (Leveridge, 2011; Leveridge and Shail, 2011). It is possible that bedding is rotated due to granite emplacement or later extensional faulting and varies at different points around the pluton (Hughes et al., 2009). Therefore, the area is considered to highlight an anomalous scenario of potentially important lineaments in the region.

Based on the bedrock analysis of the semi-automated lineaments, both slate and granite subdivisions show a consistent ESE-WNW grouping of features. It is likely that in the slate subdivision this is the result of either lineaments being detected along Variscan (late Devonian-Carboniferous) bedding-parallel faulting or the detection of recessive features in the Devonian sedimentary succession due to the interbedding of mudstone and sandstone horizons. However, sedimentary origins cannot explain the same set observed in the granite due to its magmatic nature, and the much younger Permian age. This lineament grouping is therefore considered to be caused by bedding-parallel faulting. Structures in slate have subsequently been reactivated during Permian (D3) extension, thus causing faulting of the Permian granite. This interpretation agrees with the model of Shail & Alexander (1997) where extension resulting in reactivation of earlier Variscan thrusts caused zones of distributed shear, detachments and high-angle faults. The only aspect of this theory that is difficult to reconcile is that the ESE-WNW trend observed in this study is at odds with the ENE-WSW observations further east by Shail & Alexander (1997) and the prior works of Alexander & Shail (1995, 1996) but may reflect the rotation of sedimentary rocks through faulting and granite emplacement recorded along the northern margin of the Land's End pluton (Hughes et al., 2009). It is beyond the scope of this study to investigate further but this discrepancy may be due to a number of factors such as: smaller scale ENE-WSW

structures being observable in the field; a sampling bias in either the field due to available outcrop or from the semi-automated lineament detection; or due to the different localities where data for their studies have been collected immediately to the east of this study.

Regional fault trends in granites and slates NW-SE and NNW-SSE fault systems

There is a divergence in the orientation of major fault zones between the granite and slate subdivision when analysing lineaments in the NW-SE quadrants. The granite subdivision shows a much more distinct NW-SE trend compared to the diffuse grouping observed in slate (Figure 8A-D). Additionally, the onshore slate subdivision shows a similarly distinct NW-SE trend that is observed in the granite subdivisions. The strong NW-SE trend in granite is likely to reflect later Permian faulting and the formation of mineralised lodes in the St Just Mining District (oriented NW-SE; Dines 1956) and related to a later "reactivation" episode according to Shail and Alexander (1997). In the case of the granite, the generation of NW-SE faults at this time likely created new features in the rock mass, whereas in the slate pre-existing features, such as Variscan NNW-SSE structures, are likely to have accommodated any strain resulting in reactivated fault zones. Structural inheritance influencing fault systems in this manner is not new and has been attributed to deflections in lineament orientations by a number of studies (e.g., Meixner et al., 2017; Samsu et al., 2020). The trend in onshore slate lineaments is considered to be a local effect of nearby granite, most likely at depth influencing the fracture pattern observed in what would be the roof zone of the covered pluton.

Identifying targets for fault-controlled geothermal reservoirs

The lineament networks detected and analysed in this study are key to understanding the deep geothermal fluid flow pathways in southwest England. These are aligned sub-parallel to the contemporary maximum horizontal stress that has an approximate NW-SE orientation (Heidbach et al., 2018).

In order to investigate the width of the damage zones, the regional semi-automated lineament set was first converted to a density map of structures within the orientation (α) range $120° > \alpha > 175°$ to reflect the maximum horizontal stress and most likely orientation

for open structures. This map was used in conjunction with the existing lineament sets and the raw data to identify and manually digitise structures with long strike-lengths at a fixed scale of 1:80000. This approach was necessary due to the short segments identified in the semi-automated network. The output of this manual analysis resulted in 64 major structures being identified across the study area; illustrated in Figure 9. These were used to extract lineaments from both the semi-automated and white ribbon sets within 1000 m each side of a structure and subset by their distance from a structure (s): $0 < s <= 10$ m; $10 < s <= 50$ m; $50 < s <= 100$ m; $100 < s <= 200$ m; $200 < s <= 400$ m; $400 < s <= 1000$ m. The offshore manual lineament set was not included due to its significant overlap with the semi-automated method which would bias the analysis.

INSERT FIGURE 9 (map of digitised structures)

INSERT FIGURE 10 (equal-area rose diagrams of subset lineaments)

The orientation of derived subsets for these major NW-SE structures are presented in Figure 10. The lineaments at <= 10 m from a structure in Figure 10A show a clear NW-SE to NNW-SSE likely representing the main fault system as it rotates due to changes in bedrock from granite to slate. An ESE-WNW group is also prevalent suggesting that this trend, originally observed at a regional level, may be pervasive and exist within these fault systems. Subordinate ENE-WSW and NNE-SSW lineaments are apparent. The ENE-WSW set is derived specifically from the white ribbon lineament set (see Supplementary Information), is only observable at small scales of 1:500 or less. These sets, observable at such local scales, are an important observation and may enhance cross flow between the NNE-SSW features or act as potential barriers to flow. The main trends in Figure 10B,C mimic those in Figure 10A, however, the subordinate ENE-WSW trend becomes less distinct. At distances of more than 200 m from the faults (Figure 10D-F), the NW-SE to NNW-SSE trend is slightly diminished and the large-scale regional ESE-WNW trend becomes dominant reflecting the global trend captured in Figure 4B. This suggests that damage zones around the main NW-SE faults have an approximate 100-200m width (Figure 10A-C) and contain more frequent cross-cutting features that may enhance connectivity of the fracture network.

Comparing manual and semi-automated lineaments

The three lineament networks presented in this study provide a useful comparison not only for quantifying the effectiveness of the multi-scale semi-automated method, but also for identifying sampling bias between different methods and scales. The comparison statistics for lineament numbers, area and trace length are included in Table 3.

INSERT TABLE 3 (lineament stats)

Scale and size of the area of interest

The number of lineaments for each network and the area of the mapped region of interest for each are reported with an area-normalised count to give an idea of the density of lineaments detected (Table 3). These networks are of course mapped at different scales where the highest resolution (1:500) identifies the greatest density of lineaments. This decreases significantly compared to the offshore manual lineament network mapped at 1:5000 whereas the semi-automated network shows an increase in density deposit lower equivalent resolutions of 1:10000 to 1:40000 (for pixel resolutions of 5 m to 20 m using Tobler's Rule). The increase in the semi-automated network is likely to be a function of segmented lineaments with multiple segments mapped along the trace of a single structure.

Trace length

The statistics regarding lineament length in Table 3 show marked variation between the sets. The longest lineament lengths are achieved in the offshore manual lineament set where mean lengths are approximately three times the length of those in the semi-automated lineament set. This is also reflected in the median and standard deviations for the two sets indicating that it is reasonable to suggest that the semi-automated method underestimates lineament lengths by a factor of three. Practically, several segments along a structure are often sensed so the majority of a lineament may still be captured, so perhaps the more difficult question is how much goes undetected. An empirical approach could estimate this given the difference in lineament density and compare this to trace lengths between the semi-automated and manual offshore networks, but this is considered unwise because there is no geometric or topological point of reference.

Lineament orientations

For comparison, the orientation data for each lineament set has been reproduced in Figure 11. When examining the two manual sets (Figure 11B,C), a clear NW-NNW grouping can be seen. The main modal trend for the manual offshore set is approximately 325° compared to the white ribbon set that is aligned 340°. A broad NW-SE grouping can be seen in the semi-automated lineament set (Figure 11A), however, the dominant orientation is ESE-WNW group with a modal trend of 095°.

INSERT FIGURE 11 (main rose diagrams)

The rose diagram of the semi-automated lineament network is considered to be a robust example of the true population due to the objective approach to selecting orientations during the detection phase of the algorithm. The dominance of off-trend ESE-WNW lineaments is considered genuine, although the geological source is perhaps ambiguous. The absence of this trend in both manual analyses may be due to cognitive selection bias towards major NW-SE features where ESE-WNW trends may be more subtle or not considered to represent a fault. Concerning the white ribbon lineament network, there may be a substantial physical selection bias due to the orientation of the coastline which is predominantly subparallel to the ESE-WNW trend.

Minor ENE- and NNE-trending structures have been identified in manual studies, with ENE particularly evident in the white ribbon lineament network mapped at 1:500-scale. These have previously been noted to be missing from regional onshore studies (Yeomans et al., 2019) and it may be that these structures, well-known in the Cornish mining districts to the east, are present but not detectable in the other networks. Therefore, there may be an underlying complexity to these lineament networks that requires further investigation in future reservoir characterisation studies.

Advantages and limitations of the different approaches

This study presents a new multi-scale and multi-source semi-automated lineament

detection method that allows greater detail to be captured using a semi-automated approach. This is complemented by manual analyses to compare networks and Table 4 summarises the respective advantages and limitations of the methods.

INSERT TABLE 4 (comparison table)

Networks

Manual approaches offer a more connected network, whereby lineaments are not only longer but contain more detailed branching structures with much less post-processing required. However, the synthesis of multiple large datasets is more time-consuming requiring many individual studies that are later combined. The incorporation of user-knowledge is both an advantage for linking structures and a limitation due to potential biases, but good practices can mitigate these issues (e.g., Scheiber et al., 2015; Andrews et al., 2019).

Semi-automated methods provide a means of rapid mapping across a breadth of input datasets that can be at different scales. Thus, the resultant lineament network can capture a range of detail and potentially be based on a number of source data (e.g., Yeomans et al., 2019). The trade-off with this approach is a segmented network and the requirement for significant post-processing to identify and remove false positive lineaments.

Additionally, the segmented nature of the semi-automated network therefore means that it is not optimal for detailed investigation of connectivity and reservoir modelling parameters using topological techniques (e.g., Sanderson & Nixon, 2015, 2018; Andrews et al., 2020). At present, the connected and more detailed network of manual analyses are better suited for these purposes. However, this study has demonstrated that target structures for fault-controlled geothermal reservoirs can be identified through orientation analysis and an estimate for damage zone widths can be interpreted.

Bias in semi-automated methods

One can identify apparent selection biases for semi-automated methods and how relatable

these are to established biases for manual methods (e.g., Scheiber et al., 2015; Andrews et al., 2019; Shipton et al., 2019). Both semi-automated and manual approaches are subject to physical bias in the data such as coverage and whether a lineament is observable in the data (Shipton et al. 2019). This was especially the case for lineaments manually digitised within the white ribbon due to the shape of the coastline and image shading but was problematic for the input data in semi-automated methods where structures may be discontinuous.

The OBIA method, where pixels are clustered into image objects, is for all intents and purposes an unsupervised machine learning approach and has its own algorithmic bias. The data-driven image segmentation method will successfully identify pixels representing lineaments and group these together but struggles to generalise where the signal is weak, or non-existent. This results in the generation of segments that remain unlinked and is a reflection of high bias and low variance and the bias-variance trade-off from data science transcend the analysis (Friedman,1997). To mitigate high bias, the accuracy can be reduced allowing more freedom to include weak signal, however, the variance will increase resulting in more spurious lineaments being detected which may in turn degrade the lineament network. This is an algorithmic selection bias and is the semi-automated equivalent to the cognitive selection biases that occur in manual analyses.

Remote sensing implications

It has been demonstrated in this study that lineament detection can be conducted across adjacent marine and terrestrial environments, where lineaments are represented by markedly different signatures, in a single analysis. However, it is noted that the nature of onshore and offshore data can yield different subpopulations of lineaments and the implications need to be considered. By using high-resolution bathymetry that contains areas of submerged outcrop the semi-automated lineament detection method is able to map structures that are unobservable in onshore areas. Given the large areas of submerged outcrop in this study, it is clear that simply detecting lineaments in onshore areas would give a considerably biased representation of lineaments in the region. Therefore, where applicable, particularly in coastal regions, it is recommended that bathymetric data should be included as part of an analysis where the data are available.

Conclusions

The Land's End peninsula and the surrounding offshore platforms demonstrate the complexity of the local fracture network. By using a novel multi-scale and multi-sourced semi-automated OBIA methodology to map the study area, a detailed lineament network has been established. This is complemented by manual analyses that demonstrate the limitations of the semi-automated method. We therefore conclude:

1) The incorporation of multi-scale input layers from onshore and offshore datasets allows a single, detailed, composite lineament network to be mapped rapidly over a large area (700 km^2). Despite this success, the study has highlighted the need for careful due diligence during post-processing to remove false positives that occur due to sand waves and artefacts in the data.
2) Comparison of the manual and semi-automated networks demonstrates the discrepancies in trace length of semi-automated lineaments. The segmented nature of the network means that it is inappropriate to use this directly to determine connectivity of the network for reservoir characterisation. However, orientation data is considered valuable.
3) Orientation analysis of lineaments proximal to fault zones estimate damage zone widths of 100-200 m that may be potential targets for fault-controlled geothermal reservoirs. High resolution manual mapping indicates greater complexity may exist at this scale.
4) The manual analyses demonstrate the detail available in offshore datasets whilst also filling in data gaps in the 'white ribbon' between the onshore LiDAR and bathymetry datasets.
5) Major fault zones are demonstrated to change orientation from NW-SE when hosted in granite to NNW-SSE when hosted in slate and are not proximal to the granite margin. The change in orientation is interpreted to be due to reactivation of Variscan NNW-SSE faults in the slate but the propagation of new NW-SE faults in the Permian granite.
6) Whilst semi-automated methods remain objective, they are not without bias. The study has identified algorithmic selection bias that affects the OBIA method used

here. The image segmentation technique inherently works in a data-driven manner that struggles to generalise the data in areas of poor signal. This can be mitigated by reducing accuracy (bias) but will increase variance and may degrade the lineament network.

7) Finally, the study advocates the use of bathymetry to map offshore submerged bedrock to better understand the lineament network that may be obscured in onshore areas due to cover which may cause a physical bias towards major structures.

Acknowledgements

Dr Billy Andrews and an anonymous reviewer are kindly thanked for constructive reviews that have greatly improved the structure and clarity of the manuscript. Chris Rochelle (British Geological Survey) is thanked for comments on an early draft of this manuscript. CMY is funded by a NERC Highlights grant (NE/S003886/1) on the GWatt project. Andrew Hart is thanked for helpful suggestions and comments to the final manuscript. AH is funded by a GW4+ NERC DTP grant (NE/L002434/1). CW is funded by a NERC Highlights grant (NE/S004769/1) on the GWatt project. The authors would also like to thank Adam Matthews and Harry Scott of Cornish Lithium Ltd for their support in accessing the bathymetry data. The bathymetry data used in this study have been sourced from the UK Hydrographic Office and accessed via the Admiralty Marine Data Portal. The LiDAR data used in this study have been sourced from the Centre for Ecology and Hydrology. The British Geological Survey is thanked for making the BGS Geology 625k (DiGMapGB- 625), BGS Geology 250k (DiGMap250k) and BGS Geology 50k (DiGMapGB-50) data available on an Open Government Licence.

Captions

Figure 1 Regional geology of southwest England showing the Devonian-Carboniferous sedimentary basins and Early Permian granite plutons of the Cornubian Batholith. Red box outlines area of interest for this study. The stars represent deep geothermal sites: black = United Downs; white = Eden. Contains British Geological Survey materials © UKRI 2021.

Figure 2 (**A**) Simplified geology map of the study area showing the offshore extend of the Land's End Granite pluton. Localities in this study represented by stars: 1 = Land's End; 2 = Botallack/Kenidjack Cliffs; 3 = Pendeen Cliffs, 4 = Morvah; 5 = Gurnard's Head. (**B**) Equal-area rose diagram of structures from 1:50 000 BGS fault and mineral vein data. Contains British Geological Survey materials © UKRI 2021.

Figure 3 (**A**) Workflow used for bottom-up Object-Based Image Analysis based on Yeomans et al. (2019). (**B**) Area of masked data derived from Terrain Ruggedness Index thresholding and manual mapping of sand waves.

Figure 4 (**A**) Regional map of the semi-automated lineament set derived from the multi-scale Object-Based Image Analysis. (**B**) Equal-area rose diagram showing the orientation of derived lineaments. (**C**) Inset over submerged outcrop in slate areas showing predominance of NNW-SSE features. (**D**) Inset over submerged outcrop in granite areas showing predominance of NW-SE features.

Figure 5 (**A**) Overview showing area of manual lineament mapping in offshore areas. (**B**) Equal-area rose diagram showing the orientation of derived lineaments. (**C**) Overview of the manual lineament study over the offshore submerged platform. (**D**) Inset highlighting the structural complexity of the lineament network in this area. (**E**) Small inset demonstrating mutually cross-cutting lineaments

Figure 6 (**A**) Overview showing area of high-resolution (1:500) manual lineament mapping in the ``white ribbon'' data gap based on aerial photography. (**B**) Equal-area rose diagram showing the orientation of derived lineaments. (**C**) Inset over Gurnard's Head showing an array of lineaments. (**D**) Inset showing NW-SE trending lineaments around the Pendeen Cliffs to the west of Portheras Cove that mimic the orientation of known mineralised lode systems. (**E**) Inset over Kenidjack Cliffs, between Botallack and Cape Cornwall, displaying a complex fault network with multiple orientations of lineaments. (**F**) Inset highlighting features around Land's End where NW-SE feature appear to extend from the onshore into the offshore between which lineaments do not share a similar orientation.

Figure 7 Equal-area rose diagrams reproduced from Figures 4, 5 and 6 for comparison across the three lineament sets. Lineaments are derived from (**A**) semi-automated set, (**B**) manual offshore set and (**C**) white ribbon (coastal) set.

Figure 8 Equal-area rose diagrams for subdivision of the semi-automated lineament set based on bedrock associations and their location within the onshore or offshore environment. (**A**) shows onshore lineaments in granite. (**B**) onshore lineaments in slate. (**C**) offshore lineaments in granite. (**D**) offshore lineaments in slate. Note the marked different in NW-SE oriented lineaments between onshore and offshore granite areas and the dominance and ESE-WNW trend in the latter.

Figure 9 Overview map of manually digitised major structures with an approximate NW-SE trend. Similarly oriented structures are currently being explored further east in the southwest England for fault-hosted geothermal reservoirs. These structures have been digitised based on density of lineaments oriented $120 > a > 175$, the lineament sets derived in this study and the basemap of raw tilt derivative transformed data (20 m pixels).

Figure 10 Equal-area rose diagrams for subsets of lineaments (derived from semi-automated and manual “white ribbon” lineament sets) based on radial distance away from digitised major NW-SE structures (s). (**A**) $0 < s <= 10$ m; (**B**) $10 < s <= 50$ m; (**C**) $50 < s <= 100$ m; (**D**) $100 < s <= 200$ m; (**E**) $200 < s <= 400$ m; (**F**) $400 < s <= 1000$ m. These subsets of lineaments are used to infer the presence of damage zones, approximately 100 m in width, that may act as reservoirs to geothermal fluids.

Figure 11 Equal-area rose diagrams for subdivision of the semi-automated lineament set based on bedrock associations. (**A**) shows those lineaments that are within granite rocks with a strong NW-SE trend and subordinate ESE-WNW trend. (**B**) displays lineaments within slate where the ESE-WNW dominates and a broader grouping is seen in the NW-SE quadrants.

Table 1

Breakdown of the lineaments removed during each post-processing stage, the total removed and the remaining lineaments.

Table 2

Comparison of the three lineament networks that have been collected across the study area. Semi-automated methods used a bottom-up Object-Based Image Analysis approach by Yeomans et al. (2019), the manual offshore network and white ribbon network were collected manually at a fixed scale of 1:5000 and 1:500, respectively.

Table 3

Population statistics for the count and length of lineaments across the three lineament sets where area-normalised counts have been included due to the vast difference in coverage between the three lineament sets.

Table 4

Comparison of the advantages and limitations of semi-automated and manual lineament detection methods used in this study.

References

Alexander, A. C., & Shail, R. K. (1995). Late Variscan structures on the coast between Perranporth and St. Ives, Cornwall. *Proceedings of the Ussher Society*, *8*, 398–404.

Alexander, A. C., & Shail, R. K. (1996). Late- to post-Variscan structures on the coast between Penzance and Pentewan, South Cornwall. *Proceedings of the Ussher Society*, *9*, 72–78.

Alexander, A. C., Shail, R. K., & Leveridge, B. E. (2019). Late Paleozoic extensional reactivation of the Rheic–Rhenohercynian suture zone in SW England, the English Channel and Western Approaches. *Geological Society, London, Special Publications*, *470*, SP470.19. https://doi.org/10.1144/SP470.19

Andrews, Billy J., Jennifer J. Roberts, Zoe K. Shipton, Sabina Bigi, M. Chiara Tartarello, & Gareth Johnson, (2019). How Do We See Fractures? Quantifying Subjective Bias in Fracture Data Collection. *Solid Earth,* 10, 487–516. https://doi.org/10.5194/se-10-487-2019.

Andrews, B. J., (2020). The effect of lithology, sub-bed scale heterogeneities, and mechanical stratigraphy on fault and fracture properties in coal bearing sequences. Unpublished PhD thesis, University of Strathclyde, Glasgow.

Andrews, Billy James, Zoe Kai Shipton, Richard Lord, & Lucy McKay (2020). The Growth of Faults and Fracture Networks in a Mechanically Evolving, Mechanically Stratified Rock Mass: A Case Study from Spireslack Surface Coal Mine, Scotland. *Solid Earth,* 11, 2119–40. https://doi.org/10.5194/se-11-2119-2020.

Bertrand, L., Jusseaume, J., Géraud, Y., Diraison, M., Damy, P. C., Navelot, V., & Haffen, S. (2017). Structural heritage, reactivation and distribution of fault and fracture network in a rifting context: Case study of the western shoulder of the Upper Rhine Graben. Journal of Structural Geology, 108, 243–255. https://doi.org/10.1016/j.jsg.2017.09.006

BGS Geology. (2000). *DiGRock250k digital map*. British Geological Survey.

Chen, Y., Clark, A. H., Farrar, E., Wasteneys, H. A. H. P., Hodgson, M. J., & Bromley, A. V. (1993). Diachronous and independent histories of plutonism and mineralization in the Cornubian Batholith, southwest England. *Journal of the Geological Society, London*, *150*, 1183–1191.

Chesley, J. T., Halliday, A. N., Snee, L. W., Mezger, K., Shepherd, T. J., & Scrivener, R. C. (1993). Thermochronology of the Cornubian batholith in southwest England: Implications for pluton emplacement and protracted hydrothermal mineralization. *Geochimica et Cosmochimica Acta*, *57*, 1817–1835. https://doi.org/10.1016/0016-7037(93)90115-D

Diamant, E. (2004). Top-down unsupervised image segmentation (it sounds like an oxymoron, but it actually isn't). *Proceedings of the 3rd Pattern Recognition in Remote Sensing Workshop (PRRS'04), August 2004, Kingston University, UK*.

Dines, H. G. (1956). *The Metalliferous mining region of south-west England*. Economic Memoirs of the Geological Survey of Great Britain.

Dragut, L., Tiede, D., & Levick, S. R. (2010). ESP: A tool to estimate scale parameter for multiresolution image segmentation of remotely sensed data. *International Journal of Geographical Information Science*, *24*, 859–871. https://doi.org/10.1080/13658810903174803

Eisank, C., Smith, M., & Hillier, J. (2014). Assessment of multiresolution segmentation for delimiting drumlins in digital elevation models. *Geomorphology*, *214*, 452–464. https://doi.org/10.1016/j.geomorph.2014.02.028

Evans, C. D. R. (1990). *United Kingdom offshore regional report: The Geology of the Western English Channel and its Western Approaches*. HMSO, London.

Fairhead, J. D., & Williams, S. E. (2006). Evaluating Normalized Magnetic Derivatives for Structural Mapping. *Society of Exploration Geophysicists New Orleans Extended Abstract*, 845–849. New Orleans: Society of Exploration Geophysicists.

Friedman, J. H. (1997). On Bias, Variance, 0/1-Loss, and the Curse-of-Dimensionality. *Data Mining and Knowledge Discovery*, *1*, 55–77. https://doi.org/10.1023/A:1009778005914

Gerard, F. (2014). *LIDAR QUALITY CONTROL REPORT Project: PM 1478* (Vol. 44).

Gleeson, S. A., Wilkinson, J. J., Shaw, H. F., & Herrington, R. J. (2000). Post-magmatic hydrothermal circulation and the origin of base metal mineralization, Cornwall, UK. *Journal of the Geological Society, London*, *157*, 589–600. https://doi.org/10.1144/jgs.157.3.589

Gleeson, S. A., Wilkinson, J. J., Stuart, F. M., & Banks, D. A. (2001). The origin and evolution of base metal mineralising brines and hydrothermal fluids, South Cornwall, UK. *Geochimica et Cosochimica Acta*, *65*, 2067–2079.

Goode, A. J. J., & Taylor, R. T. (1988). *Geology of the area around Penzance*. Memoir of the British Geological Survey, Sheet 351 and 358 (England and Wales).

Healy, M. G. (1996). Late Quaternary Coastal Change in West Cornwall, UK. In M. G. Healy (Ed.), *Late Quaternary Coastal Change in West Cornwall, UK*. Durham: Environmental Research Centre the University of Durham.

Heidbach, O., Rajabi, M., Cui, X., Fuchs, K., Müller, B., Reinecker, J., … Zoback, M. (2018). The World Stress Map database release 2016: Crustal stress pattern across scales. *Tectonophysics*, *744*, 484–498. https://doi.org/10.1016/j.tecto.2018.07.007

Holloway, S., & Chadwick, R. A. (1986). The Sticklepath-Lustleigh fault zone: Tertiary sinistral reactivation of a Variscan dextral strike-slip fault. *Journal of the Geological Society, London*, *143*, 447–452.

Hughes, S. P., Stickland, R. J., Shail, R. K., LeBoutillier, N. G., Alexander, A. C., & Thomas, M. (2009). The chronology and kinematics of Late Palaeozoic deformation in the NW contact metamorphic aureole of the Land's End Granite. Geoscience in South-West England, 12, 140–152.

Karimi, B., & Karimi, H. A. (2017). An automated method for the detection of topographic patterns at tectonic boundaries. *The Ninth International Conferences on Pervasive Patterns and Applications*, 72–77.

Leon, J. X., Phinn, S. R., Hamylton, S., & Saunders, M. I. (2013). Filling the “white ribbon” - a multisource seamless digital elevation model for Lizard Island, northern Great Barrier Reef. *International Journal of Remote Sensing*, *34*, 6337–6354. https://doi.org/10.1080/01431161.2013.800659

Leveridge, B. E. (2011). The Looe, South Devon and Tavy basins: the Devonian rifted passive margin successions. *Proceedings of the Geologists’ Association*, *122*, 616–717. https://doi.org/10.1016/j.pgeola.2011.03.005

Leveridge, B. E., & Hartley, A. J. (2006). The Varisan Orogeny: the development and deformation of Devonian/Carboniferous basins in SW England and South Wales. In P. J. Brenchley & P. F. Rawson (Eds.), *The Geology of England and Wales* (2nd ed., pp. 225–256). The Geological Society, London.

Leveridge, B. E., & Shail, R. K. (2011). The Gramscatho Basin, south Cornwall, UK: Devonian active margin successions. *Proceedings of the Geologists’ Association*, *122*, 568–615. https://doi.org/10.1016/j.pgeola.2011.03.004

Marpu, P. R., Niemeyer, I., Nussbaum, S., & Gloaguen, R. (2008). A procedure for automatic object-based classification. In T. Blaschke, S. Lang, & G. J. Hay (Eds.), *Object-Based Image Analysis: Spatial Concepts for Knowledge-Driven Remote Sensing Applications* (pp. 169–184). https://doi.org/10.1007/978-3-540-77058-9

Mason, T., McVey, S., & Rainbow, B. (2008). Colouring the “White Ribbon”: Strategic Coastal Monitoring in the South-East of England. *Hydro International*. Retrieved from https://www.hydro-international.com/content/article/colouring-the-white-ribbon

Masoud, A. A., & Koike, K. (2011). Auto-detection and integration of tectonically significant lineaments from SRTM DEM and remotely-sensed geophysical data. *ISPRS Journal of Photogrammetry and Remote Sensing*, *66*, 818–832. https://doi.org/10.1016/j.isprsjprs.2011.08.003

Masoud, A., & Koike, K. (2006). Tectonic architecture through Landsat-7 ETM+/SRTM DEM-derived lineaments and relationship to the hydrogeologic setting in Siwa region, NW Egypt. *Journal of African Earth Sciences*, *45*, 467–477. https://doi.org/10.1016/j.jafrearsci.2006.04.005

Masoud, A., & Koike, K. (2017). Applicability of computer-aided comprehensive tool (LINDA: LINeament Detection and Analysis) and shaded digital elevation model for characterizing and interpreting morphotectonic features from lineaments. *Computers & Geosciences*, *106*,

89–100.

Mavrantza, O. D., & Argialas, D. P. (2006). Object-oriented image analysis for the identification of geologic lineaments. *International Archives of Photogrammetry, Remote Sensing and Spatial Information Sciences*, *36*, 1–6.

Meixner, J., Grimmer, J. C., Becker, A., Schill, E., & Kohl, T. (2017). Comparison of different digital elevation models and satellite imagery for lineament analysis: Implications for identification and spatial arrangement of fault zones in crystalline basement rocks of the southern Black Forest (Germany). *Journal of Structural Geology*, *108*, 256–268. https://doi.org/10.1016/j.jsg.2017.11.006

Middleton, M., Schnur, T., Sorjonen-ward, P., & Hyvönen, E. (2015). Geological lineament interpretation using the Object-Based Image Analysis Approach: results of semi-automated analyses versus visual interpretation. *Geological Survey of Finland, Special Paper*, *57*, 135–154.

Miller, H. G., & Singh, V. (1994). Potential field tilt - a new concept for location of potential field sources. *Journal of Applied Geophysics*, *32*, 213–217. https://doi.org/10.1016/0926-9851(94)90022-1

Nixon, C. W., Sanderson, D. J., & Bull, J. M. (2012). Analysis of a strike-slip fault network using high resolution multibeam bathymetry, offshore NW Devon U.K. *Tectonophysics*, *541–543*, 69–80. https://doi.org/10.1016/j.tecto.2012.03.021

O'Leary, D. W., Friedman, J. D., & Pohn, H. A. (1976). Lineament, linear, lineation: Some proposed new standards for old terms. *Geological Society Of America Bulletin*, *87*, 1463–1469. https://doi.org/10.1130/0016-7606(1976)87<1463

Rahnama, M., & Gloaguen, R. (2014). TecLines: A MATLAB-Based Toolbox for Tectonic Lineament Analysis from Satellite Images and DEMs, Part 1: Line Segment Detection and Extraction. *Remote Sensing*, *6*, 5938–5958. https://doi.org/10.3390/rs6075938

Rahnama, M., & Gloaguen, R. (2014). TecLines: A MATLAB-based toolbox for tectonic lineament analysis from satellite images and DEMs, Part 2: Line Segments Linking and Merging. *Remote Sensing*, *6*, 11468–11493. https://doi.org/10.3390/rs61111468

Rutzinger, M., Maukisch, M., & Petrini-Monteferri, F. (2007). Development of Algorithms for the Extraction of Linear Patterns (Lineaments) from Airborne Laser Scanning Data. *Proceedings of the Conference "Geomorphology for the Future", Obergurgl, 2007*, 1–8.

Samsu, A., Cruden, A. R., Micklethwaite, S., Grose, L., & Vollgger, S. A. (2020). Scale matters:

The influence of structural inheritance on fracture patterns. *Journal of Structural Geology*, *130*, 103896. https://doi.org/10.1016/j.jsg.2019.103896

Sanderson, D. J., Dix, J. K., Westhead, K. R., & Collier, J. S. (2017). Bathymetric mapping of the coastal and offshore geology and structure of the Jurassic Coast, Weymouth Bay, UK. *Journal of the Geological Society*, *174*, 498–508. https://doi.org/10.1144/jgs2016-070

Sanderson, D. J., & Peacock, D. C. P. (2020). Making rose diagrams fit-for-purpose. *Earth-Science Reviews*, *201*, 103055. https://doi.org/10.1016/j.earscirev.2019.103055

Scheiber, T., Fredin, O., Viola, G., Jarna, A., Gasser, D., & Łapińska-Viola, R. (2015). Manual extraction of bedrock lineaments from high-resolution LiDAR data: methodological bias and human perception. *Journal of the Geological Society of Sweden (GFF)*, *137*, 362–372. https://doi.org/10.1080/11035897.2015.1085434

Scrivener, R. C. (2006). Cornubian granites and mineralization of SW England. In P. J. Brenchley & P. F. Rawson (Eds.), *The Geology of England and Wales* (Second, pp. 257–268). The Geological Society, London.

Scrivener, R. C., Darbyshire, D. P. F., & Shepherd, T. J. (1994). Timing and significance of crosscourse mineralization in SW England. *Journal of the Geological Society, London*, *151*, 587–590.

Shail, R. K., & Alexander, A. C. (1997). Late Carboniferous to Triassic reactivation of Variscan basement in the western English Channel: evidence from onshore exposures in south Cornwall. *Journal of the Geological Society, London*, *154*, 163–168. https://doi.org/10.1144/gsjgs.154.1.0163

Shail, R. K., & Leveridge, B. E. (2009). The Rhenohercynian passive margin of SW England: Development, inversion and extensional reactivation. *Comptes Rendus Geoscience*, *341*, 140–155.

Šilhavý, J., Minár, J., Mentlík, P., & Sládek, J. (2016). A new artefacts resistant method for automatic lineament extraction using Multi-Hillshade Hierarchic Clustering (MHHC). *Computers & Geosciences*, *92*, 9–20.

Simons, B., Shail, R. K., & Andersen, J. C. Ø. (2016). The petrogenesis of the Early Permian Variscan granites of the Cornubian Batholith: Lower plate post-collisional peraluminous magmatism in the Rhenohercynian Zone of SW England. *Lithos*, *260*, 76–94. https://doi.org/10.1016/j.lithos.2016.05.010

Sukumar, M., Venkatesan, N., & Babu, C. N. K. (2014). A review of various lineament

detection techniques for high resolution satellite images. *International Journal of Advanced Research in Computer Science and Software Engineering*, *4*(3), 72–78.

Thiele, S. T., Grose, L., Samsu, A., Micklethwaite, S., Vollgger, S. A., & Cruden, A. R. (2017). Rapid, semi-automatic fracture and contact mapping for point clouds, images and geophysical data. *Solid Earth*, *8*, 1241–1253. https://doi.org/10.5194/se-8-1241-2017

Verduzco, B., Fairhead, D., Green, C. M., & MacKenzie, C. (2004). New insights into magnetic derivatives for structural mapping. *The Meter Reader*, 116–119.

Waller, M. P., & Long, A. J. (2003). Holocene coastal evolution and sea-level change on the southern coast of England: A review. *Journal of Quaternary Science*, *18*, 351–359. https://doi.org/10.1002/jqs.754

Westhead, R. K., McCarthy, D. J., Collier, J. S., & Sanderson, D. J. (2018). Spatial variability of the Purbeck–Wight Fault Zone—a long-lived tectonic element in the southern UK. *Proceedings of the Geologists' Association*, *129*, 436–451. https://doi.org/10.1016/j.pgeola.2017.08.005

Yeomans, C. M., Middleton, M., Shail, R. K., Grebby, S., & Lusty, P. A. J. (2019). Integrated Object-Based Image Analysis for semi-automated geological lineament detection in southwest England. *Computers & Geosciences*, *123*, 137-148 [Available Online November 2018]. https://doi.org/10.1016/j.cageo.2018.11.005

Yeomans, C. M., Head, M., & Lindsay, J. J. 2021. Application of the tilt derivative transform to bathymetric data for structural lineament mapping. *Journal of Structural Geology*, *146*, 104301. https://doi.org/10.1016/j.jsg.2021.104301

Figure 1

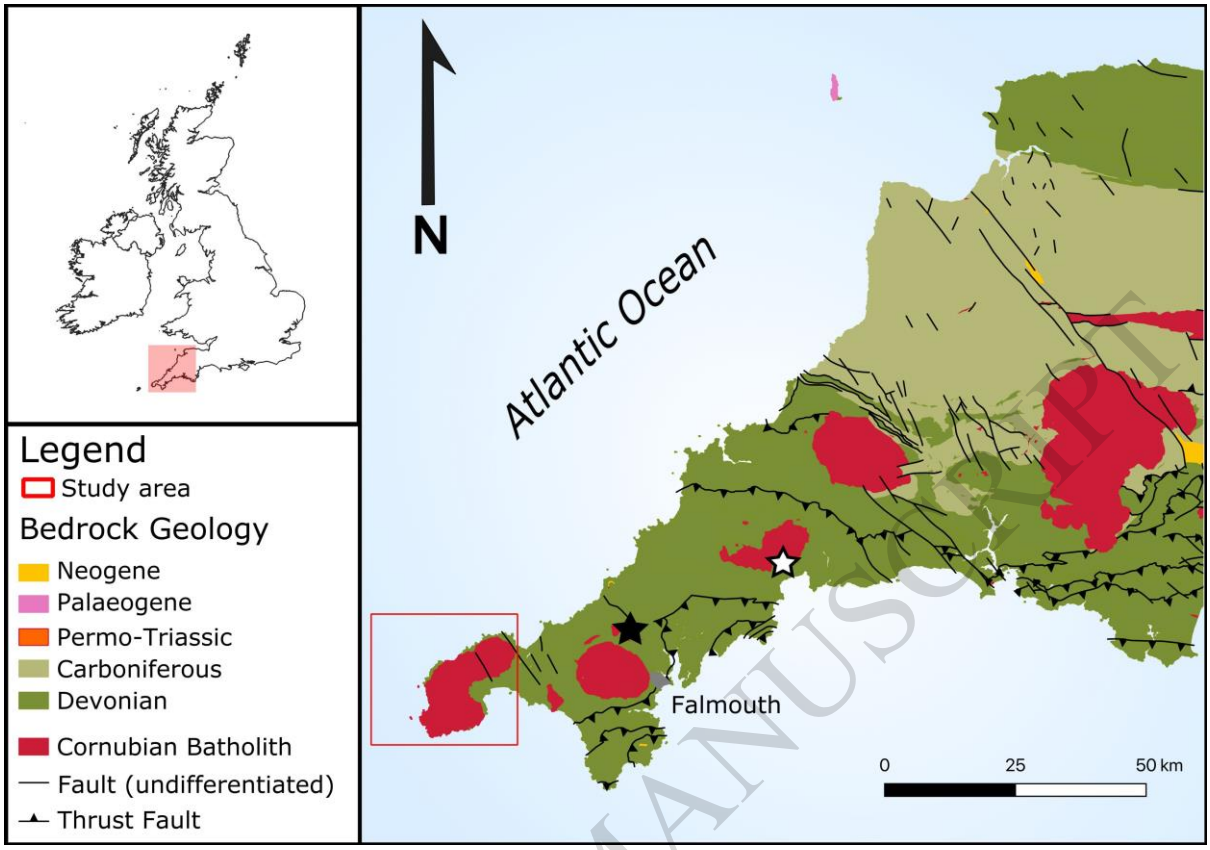

Figure 2

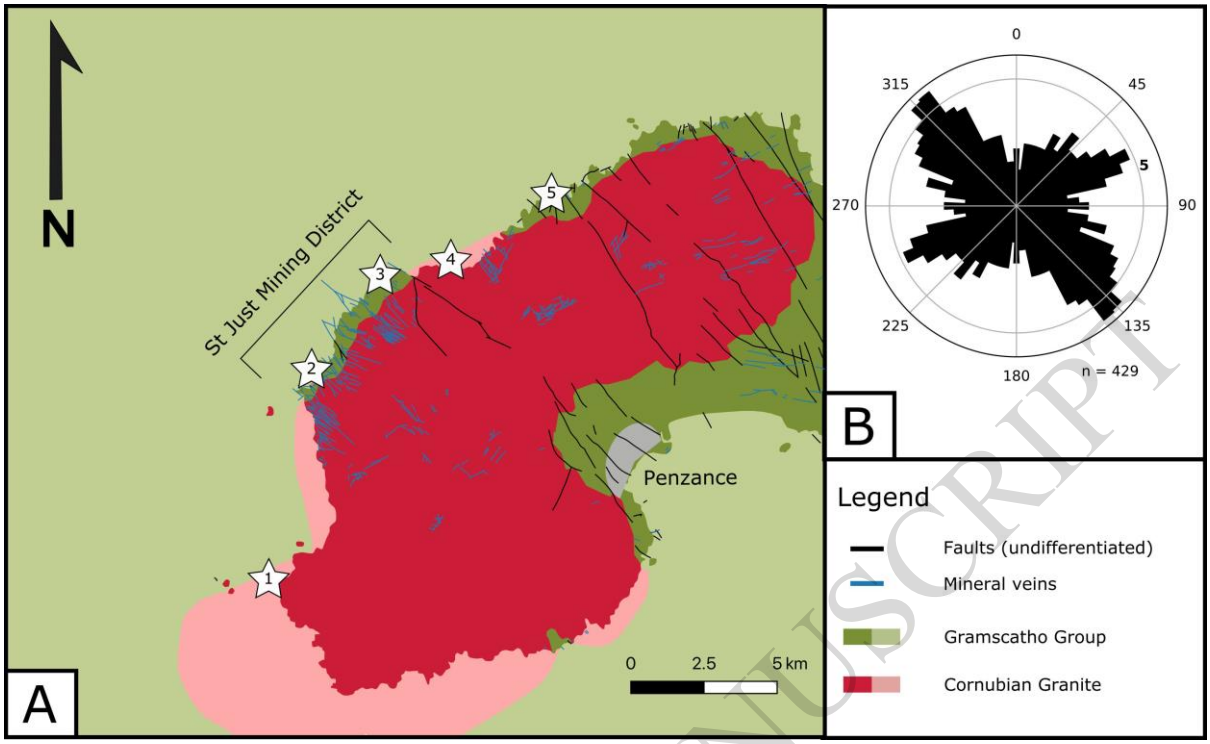

Figure 3

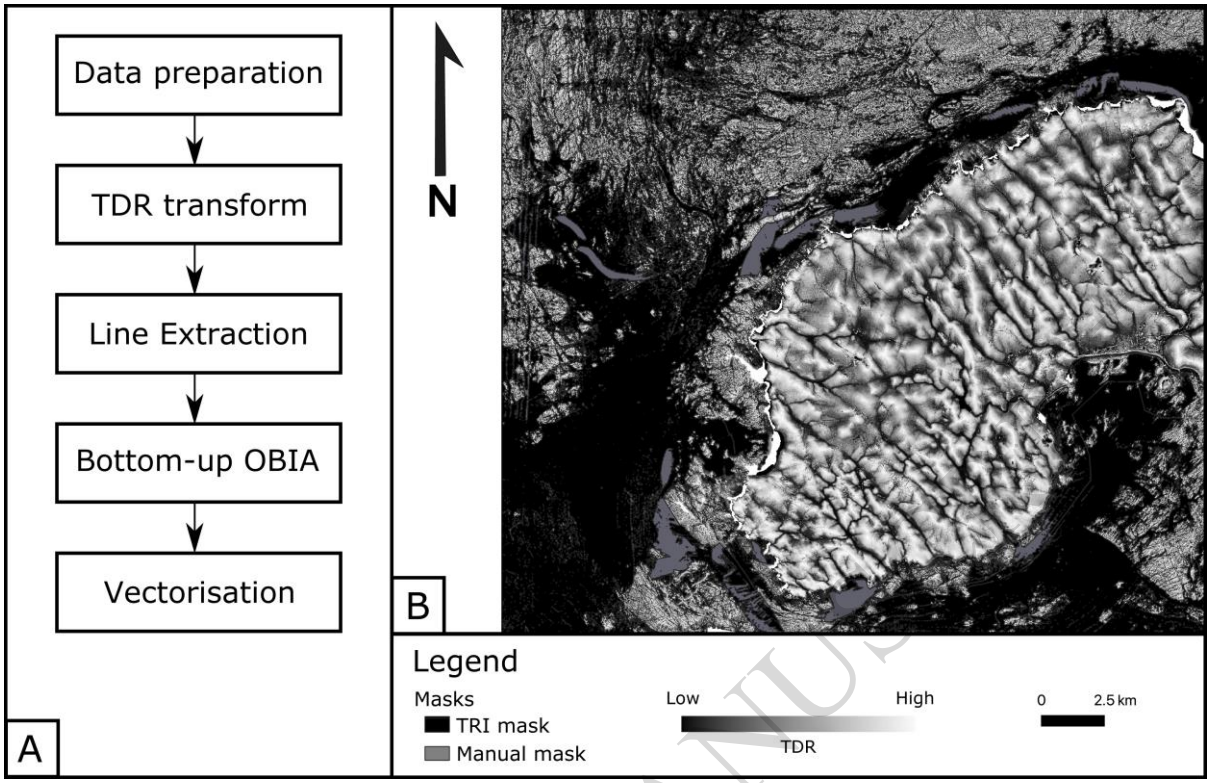

Figure 4

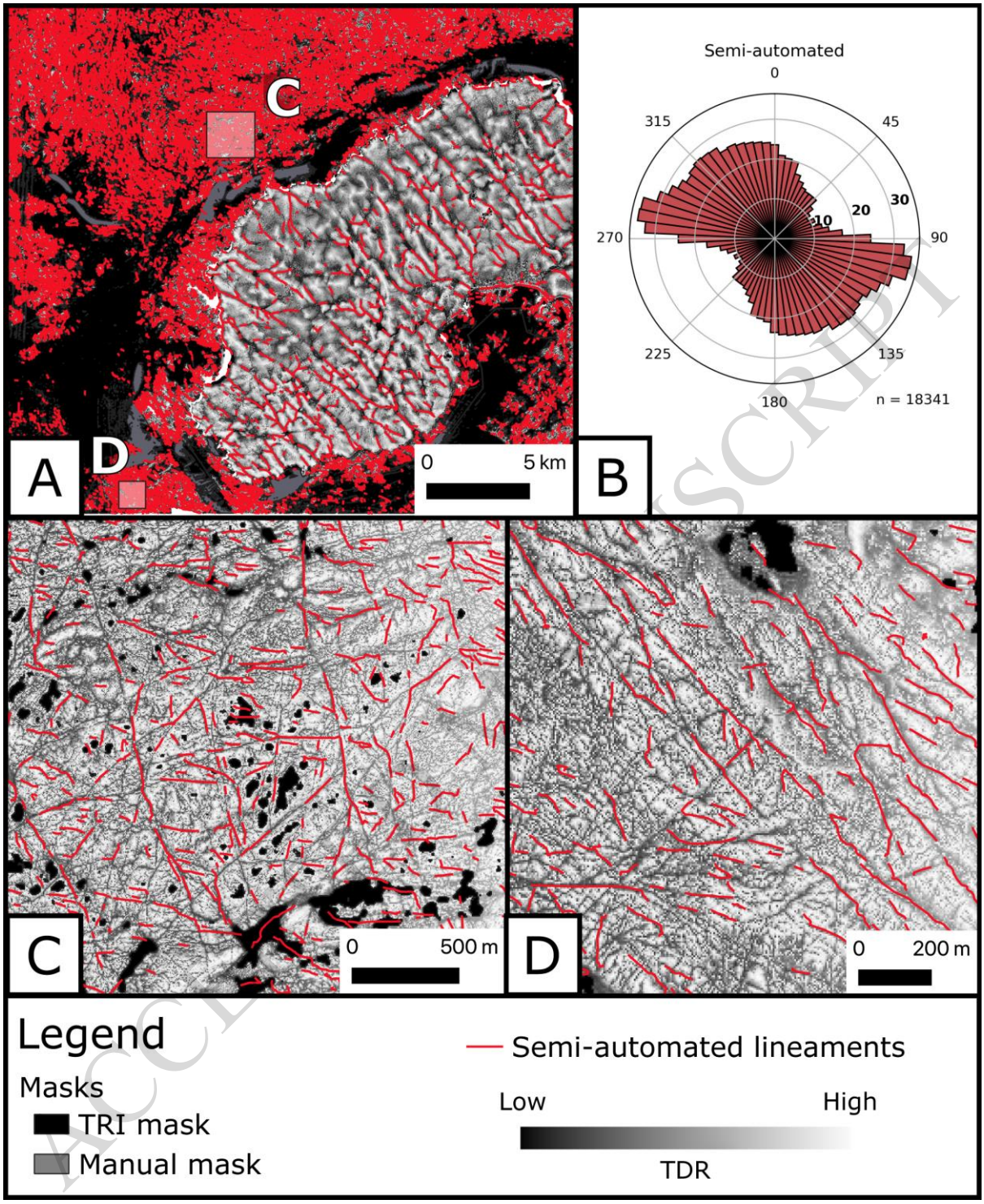

Figure 5

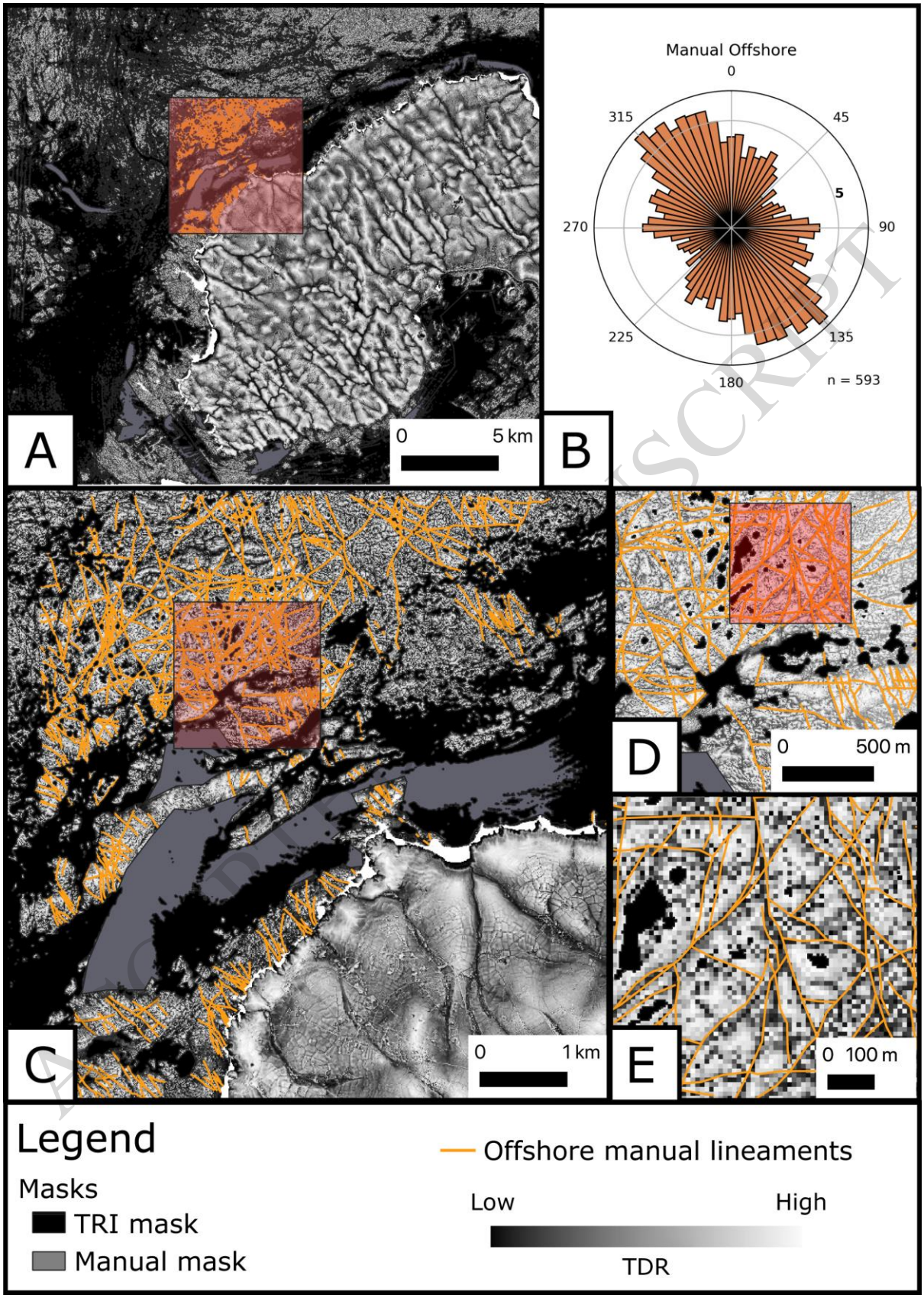

Figure 6

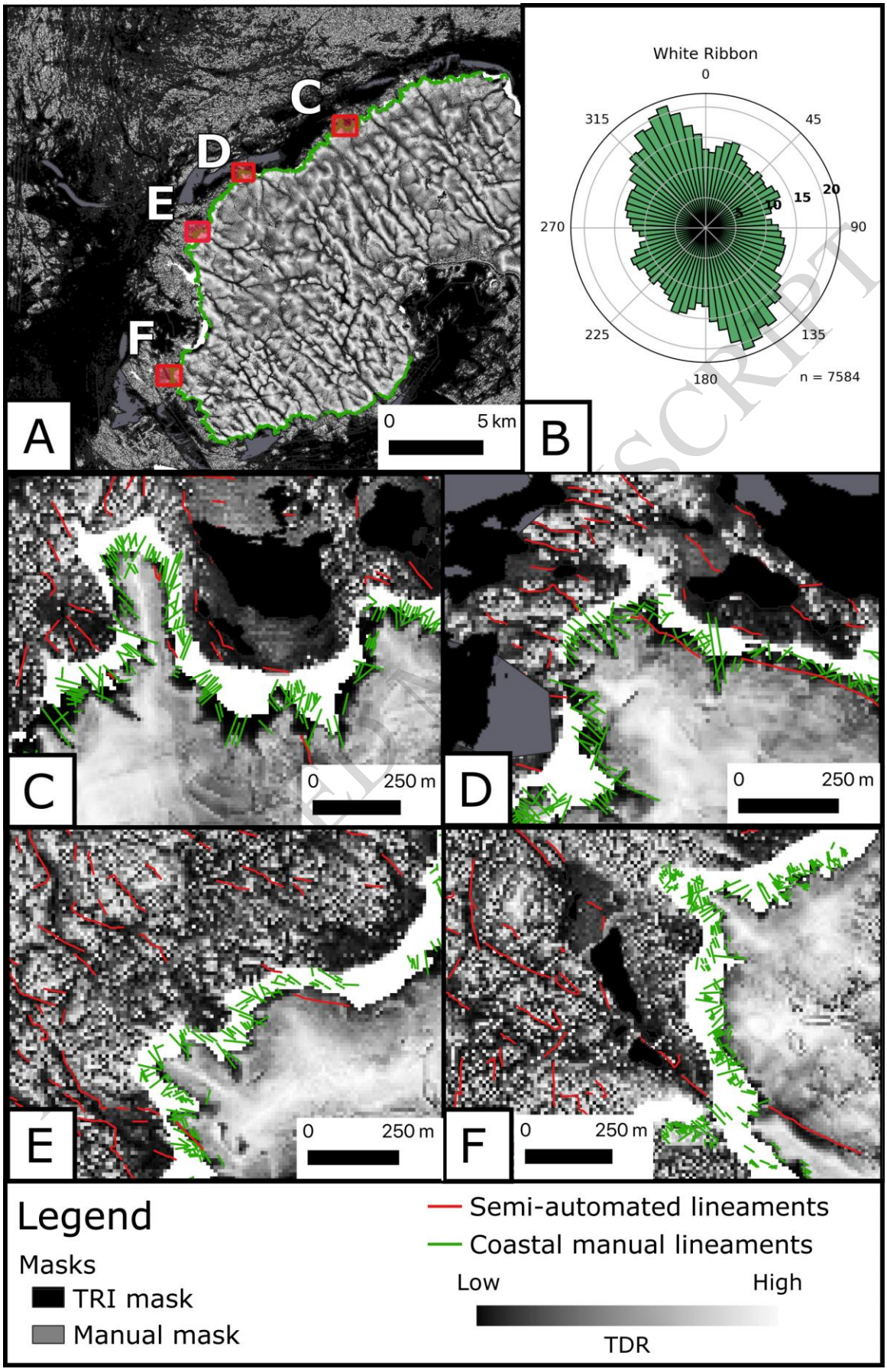

Figure 7

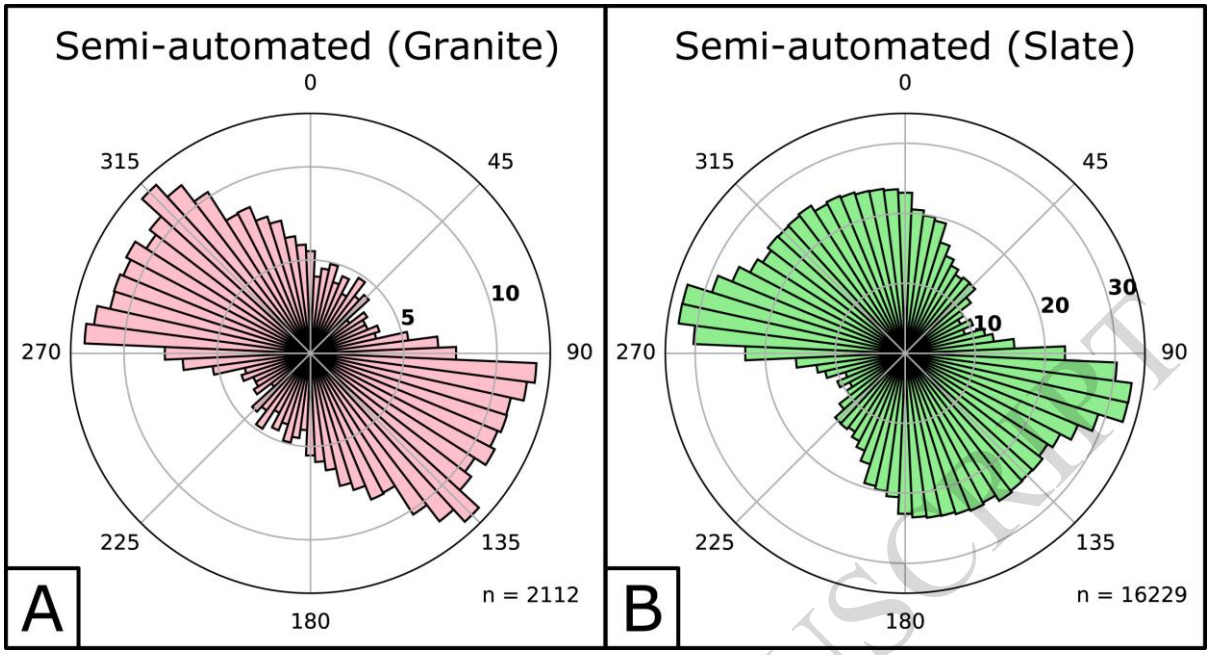

Figure 8

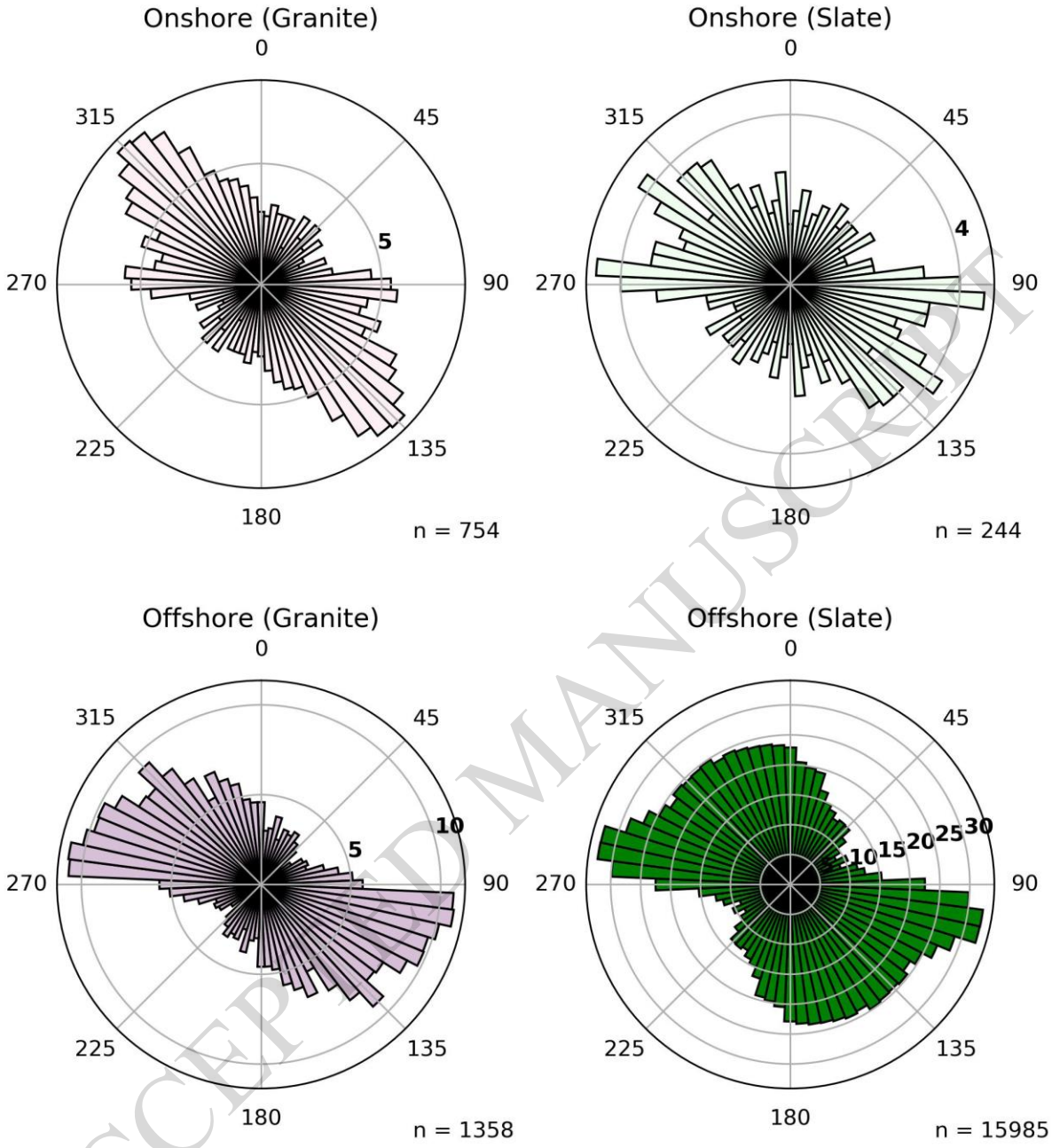

Figure 9

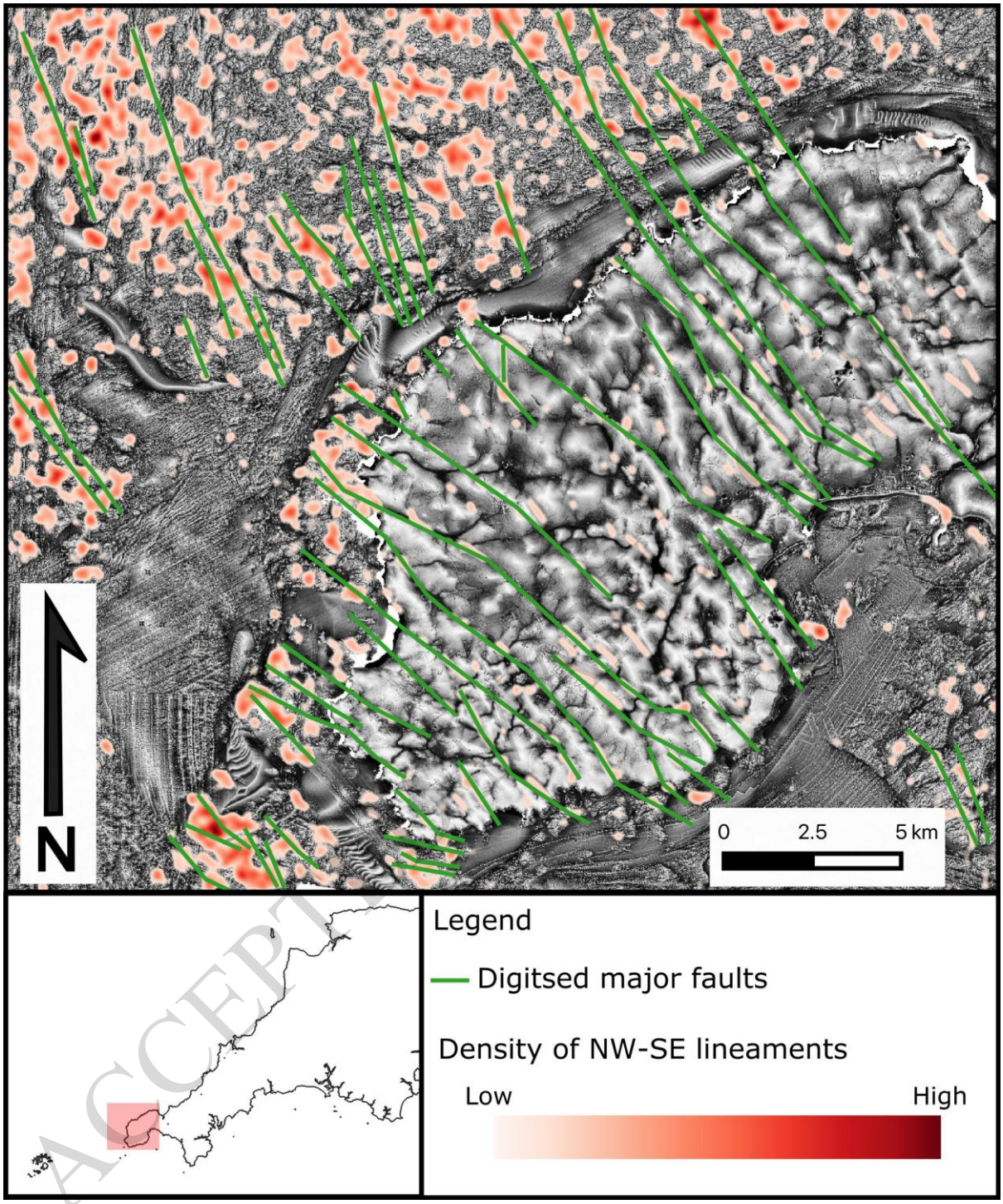

Figure 10

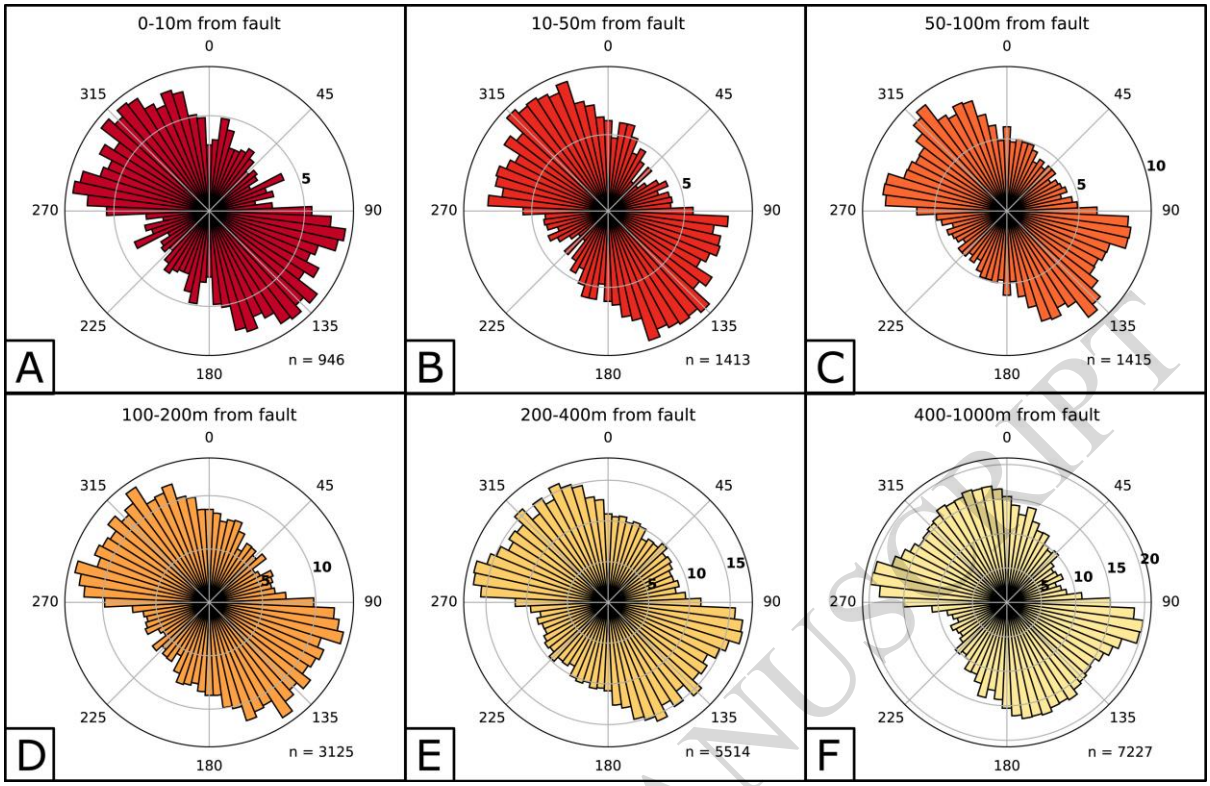

Figure 11

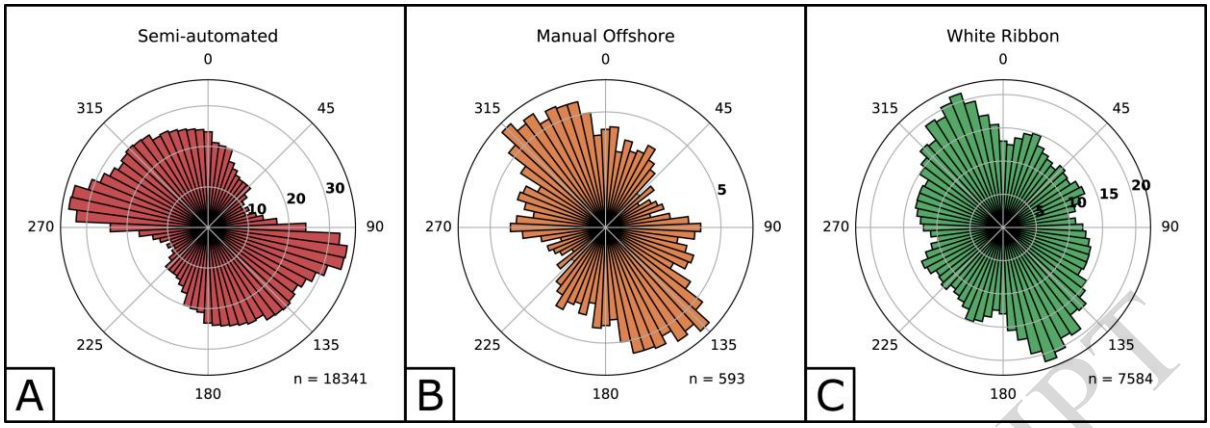

Table 1

	No data	TRI mask	Sand wave mask	Manual step	Field boundaries
Removed lineaments	12	8046	1189	95	667
Total removed lineaments	10009				
Remaining lineaments	18341				

Table 2

Method	Lineament Orientations	General Comments
Semi-automated	E-ESE trend that dominates the population followed by a second more diffuse NW-N grouping and minor NE-trending contribution	1) Bathymetry shows higher density of lineaments compared to onshore area. 2) The method does not capture all lineaments but generally identifies at least one segment along each structure
Offshore Manual	Lineaments predominately trend NW-NNW with a subordinate NNE-NE group present and also a clear sub-population of E-W trending lineaments. ENE-WSW lineaments are notably few in number.	1) The subset is only a small representation of study area. 2) Predominant orientation of NNW-trending lineaments but NE-trending features are also prominent. 3) Both main sets appear to mutually cross-cut each other suggesting multiple reactivation episodes
White Ribbon	Dominant trend of NNW-oriented lineaments but shows that all other orientations have some degree of representation in the lineament set	1) The main trend is surprisingly well-defined in its NNW orientation. 2) Presence of lineaments in most orientations implies greater complexity. 3) Likely to inlcude significant physical selection bias due to coastline

Table 3

Lineament set	Count	Area (sq km)	Area-normalised count	Mean	Standard deviation	Median	Range	Skewness	Kurtosis
Semi-automated	18341	700	26.20	100.47	98.88	71.93	2287.74	4.94	50.49
Offshore Manual	593	49	12.10	315.70	327.11	216.38	2575.90	3.48	15.77
White Ribbon	7584	37.21	203.82	26.09	19.25	20.95	234.17	2.80	14.19

Table 4

	Advantages	Limitations
Semi-automated methods	Rapid mapping over large areas, multiple input datasets, objective approach, data-driven	Segmented network, removal of false positives, prone to physical and algorithmic selection bias
Manual methods	Connected network, incorporate user-knowledge, minimal post-processing, knoweldge-driven	Time-consuming digitisation, subjective based on user-knowledge, prone to cognitive and physical selection biases